

Considerations and recommendations from the ISMRM Diffusion Study Group for preclinical diffusion MRI: Part 2 — *Ex vivo* imaging: added value and acquisition

Kurt G Schilling^{1,2,#}, Francesco Grussu^{3,4}, Andrada Ianus⁵, Brian Hansen⁶, Amy FD Howard^{7,8}, Rachel L C Barrett^{9,10}, Manisha Aggarwal¹¹, Stijn Michielse¹², Fatima Nasrallah¹³, Warda Syeda¹⁴, Nian Wang^{15,16}, Jelle Veraart¹⁷, Alard Roebroeck¹⁸, Andrew F Bagdasarian^{19,20}, Cornelius Eichner²¹, Farshid Sepehrband²², Jan Zimmermann²³, Lucas Soustelle²⁴, Christien Bowman^{25,26}, Benjamin C Tendler²⁷, Andreea Hertanu²⁸, Ben Jeurissen^{29,30}, Marleen Verhoye^{25,26}, Lucio Frydman³¹, Yohan van de Looij³², David Hike^{19,20}, Jeff F Dunn^{33,34,35}, Karla Miller⁸, Bennett A Landman³⁶, Noam Shemesh⁵, Adam Anderson^{37,2}, Emilie McKinnon³⁸, Shawna Farquharson³⁹, Flavio Dell' Acqua⁴⁰, Carlo Pierpaoli⁴¹, Ivana Drobnyak⁴², Alexander Leemans⁴³, Kevin D Harkins^{1,2,44}, Maxime Descoteaux^{45,46}, Duan Xu⁴⁷, Hao Huang^{48,49}, Mathieu D Santin^{50,51}, Samuel C. Grant^{19,20}, Andre Obenaus^{52,53}, Gene S Kim⁵⁴, Dan Wu⁵⁵, Denis Le Bihan^{56,57}, Stephen J Blackband^{58,59,60}, Luisa Ciobanu⁶¹, Els Fieremans⁶², Ruiliang Bai^{63,64}, Trygve B Leergaard⁶⁵, Jiangyang Zhang⁶⁶, Tim B Dyrby^{67,68}, G Allan Johnson^{69,70}, Julien Cohen-Adad^{71,72,73}, Matthew D Budde^{74,75}, Ileana O Jelescu^{28,76,#}

#Corresponding authors — kurt.g.schilling.1@vumc.org, ileana.jelescu@chuv.ch

¹Radiology and Radiological Sciences, Vanderbilt University Medical Center, Nashville, TN, USA, ²Vanderbilt University Institute of Imaging Science, Vanderbilt University, Nashville, TN, ³Radiomics Group, Vall d'Hebron Institute of Oncology, Vall d'Hebron Barcelona Hospital Campus, Barcelona, Spain, ⁴Queen Square MS Centre, Queen Square Institute of Neurology, Faculty of Brain Sciences, University College London, London, UK, ⁵Champalimaud Research, Champalimaud Foundation, Lisbon, Portugal, ⁶Center of Functionally Integrative Neuroscience, Aarhus University, Aarhus, Denmark, ⁷Department of Bioengineering, Imperial College London, London, UK, ⁸FMRIB Centre, Wellcome Centre for Integrative Neuroimaging, Nuffield Department of Clinical Neurosciences, University of Oxford, Oxford, United Kingdom, ⁹Department of Neuroimaging, Institute of Psychiatry, Psychology and Neuroscience, King's College London, London, UK, ¹⁰NatBrainLab, Department of Forensics and Neurodevelopmental Sciences, Institute of Psychiatry, Psychology and Neuroscience, King's College London, London, UK, ¹¹Russell H. Morgan Department of Radiology and Radiological Science, Johns Hopkins University School of Medicine, Baltimore, MD, USA, ¹²Department of Neurosurgery, School for Mental Health and Neuroscience (MHeNS), Maastricht University Medical Center, Maastricht, The Netherlands, ¹³The Queensland Brain Institute, The University of Queensland, Queensland, Australia, ¹⁴Melbourne Neuropsychiatry Centre, The University of Melbourne, Parkville, Victoria, Australia, ¹⁵Department of Radiology and Imaging Sciences, Indiana University, IN, USA, ¹⁶Stark Neurosciences Research Institute, Indiana University School of Medicine, IN, USA, ¹⁷Center for Biomedical Imaging, NYU Grossman School of Medicine, New York, NY, USA, ¹⁸Faculty of psychology and Neuroscience, Maastricht University, Maastricht, Netherlands, ¹⁹Department of Chemical & Biomedical Engineering, FAMU-FSU College of Engineering, Florida State University, Tallahassee, FL, USA, ²⁰Center for Interdisciplinary Magnetic Resonance, National High Magnetic Field

Laboratory, Tallahassee, FL, USA, ²¹Department of Neuropsychology, Max Planck Institute for Human Cognitive and Brain Sciences, Leipzig, Germany, ²²USC Stevens Neuroimaging and Informatics Institute, Keck School of Medicine of USC, University of Southern California, Los Angeles, CA, USA, ²³Department of Neuroscience, Center for Magnetic Resonance Research, University of Minnesota, MN, USA, ²⁴Aix Marseille Univ, CNRS, CRMBM, Marseille, France, ²⁵Bio-Imaging Lab, Faculty of Pharmaceutical, Biomedical and Veterinary Sciences, University of Antwerp, Antwerp, Belgium, ²⁶ μ NEURO Research Centre of Excellence, University of Antwerp, Antwerp, Belgium, ²⁷Wellcome Centre for Integrative Neuroimaging, FMRIB, Nuffield Department of Clinical Neurosciences, University of Oxford, United Kingdom, ²⁸Department of Radiology, Lausanne University Hospital and University of Lausanne, Lausanne, Switzerland, ²⁹imec Vision Lab, Dept. of Physics, University of Antwerp, Belgium, ³⁰Lab for Equilibrium Investigations and Aerospace, Dept. of Physics, University of Antwerp, Belgium, ³¹Department of Chemical and Biological Physics, Weizmann Institute of Science, Rehovot, Israel, ³²Division of Child Development & Growth, Department of Pediatrics, Gynaecology & Obstetrics, School of Medicine, Université de Genève, Genève, Switzerland, ³³Department of Radiology, Cumming School of Medicine, University of Calgary, Calgary, Alberta, Canada, ³⁴Hotchkiss Brain Institute, Cumming School of Medicine, University of Calgary, Calgary, Alberta, Canada, ³⁵Alberta Children's Hospital Research Institute, Cumming School of Medicine, University of Calgary, Calgary, Alberta, Canada, ³⁶Department of Electrical and Computer Engineering, Vanderbilt University,, ³⁷Department of Radiology and Radiological Sciences, Vanderbilt University Medical Center, Nashville, TN, USA, ³⁸Medical University of South Carolina, Charleston, SC, USA, ³⁹National Imaging Facility, The University of Queensland, Brisbane, Australia, ⁴⁰Department of Forensic and Neurodevelopmental Sciences, King's College London, London, UK, ⁴¹Laboratory on Quantitative Medical imaging, NIBIB, National Institutes of Health, Bethesda, MD, USA, ⁴²Department of Computer Science, University College London, London, UK, ⁴³PROVIDI Lab, Image Sciences Institute, University Medical Center Utrecht, The Netherlands, ⁴⁴Biomedical Engineering, Vanderbilt University, Nashville, TN, ⁴⁵Sherbrooke Connectivity Imaging Lab (SCIL), Computer Science department, Université de Sherbrooke, ⁴⁶Imeka Solutions, ⁴⁷Department of Radiology and Biomedical Imaging, University of California San Francisco, CA, USA, ⁴⁸Department of Radiology, Perelman School of Medicine, University of Pennsylvania, Philadelphia, PA, USA, ⁴⁹Department of Radiology, Children's Hospital of Philadelphia, Philadelphia, PA, USA, ⁵⁰Centre for NeuroImaging Research (CENIR), Inserm U 1127, CNRS UMR 7225, Sorbonne Université, Paris, France, ⁵¹Paris Brain Institute, Paris, France, ⁵²Department of Pediatrics, University of California Irvine, Irvine CA USA, ⁵³Preclinical and Translational Imaging Center, University of California Irvine, Irvine CA USA, ⁵⁴Department of Radiology, Weill Cornell Medical College, New York, NY, USA, ⁵⁵Key Laboratory for Biomedical Engineering of Ministry of Education, College of Biomedical Engineering & Instrument Science, Zhejiang University, Hangzhou, China, ⁵⁶CEA, DRF, JOLIOT, NeuroSpin, Gif-sur-Yvette, France, ⁵⁷Université Paris-Saclay, Gif-sur-Yvette, France, ⁵⁸Department of Neuroscience, University of Florida, Gainesville, FL, United States, ⁵⁹McKnight Brain Institute, University of Florida, Gainesville, FL, United States, ⁶⁰National High Magnetic Field Laboratory, Tallahassee, FL, United States, ⁶¹NeuroSpin, UMR CEA/CNRS 9027, Paris-Saclay University, Gif-sur-Yvette, France, ⁶²Department of Radiology, New York University Grossman School of Medicine, New York, NY, USA, ⁶³Interdisciplinary Institute of Neuroscience and Technology, School of Medicine, Zhejiang University, Hangzhou, China, ⁶⁴Frontier Center of Brain Science and Brain-machine Integration, Zhejiang University, ⁶⁵Department of Molecular Biology, Institute of Basic Medical Sciences, University of Oslo, Norway, ⁶⁶Department of Radiology, New York University School of Medicine, NY, NY, USA, ⁶⁷Danish Research Centre for Magnetic Resonance, Centre for Functional and Diagnostic Imaging and Research, Copenhagen University Hospital Amager & Hvidovre, Hvidovre, Denmark, ⁶⁸Department of Applied Mathematics and Computer Science, Technical University of Denmark, Kongens Lyngby, Denmark, ⁶⁹Duke Center for In Vivo Microscopy, Department of Radiology, Duke University, Durham, North Carolina, ⁷⁰Department of Biomedical Engineering, Duke University, Durham, North Carolina, ⁷¹NeuroPoly Lab, Institute of Biomedical Engineering, Polytechnique Montreal, Montreal, QC, Canada, ⁷²Functional Neuroimaging Unit, CRIUGM, University of Montreal, Montreal, QC, Canada, ⁷³Mila - Quebec AI Institute, Montreal, QC, Canada, ⁷⁴Department of Neurosurgery, Medical College of Wisconsin, Milwaukee, Wisconsin, ⁷⁵Clement J Zablocki VA Medical Center, Milwaukee, Wisconsin, ⁷⁶CIBM Center for Biomedical Imaging, Ecole Polytechnique Fédérale de Lausanne, Lausanne, Switzerland

Abstract

The value of preclinical diffusion MRI (dMRI) is substantial. While dMRI enables *in vivo* non-invasive characterization of tissue, *ex vivo* dMRI is increasingly being used to probe tissue microstructure and brain connectivity. *Ex vivo* dMRI has several experimental advantages including higher signal-to-noise ratio (SNR) and spatial resolution compared to *in vivo* studies, and enabling more advanced diffusion contrasts for improved microstructure and connectivity characterization. Another major advantage of *ex vivo* dMRI is the direct comparison with histological data, as a crucial methodological validation. However, there are a number of considerations that must be made when performing *ex vivo* experiments. The steps from tissue preparation, image acquisition and processing, and interpretation of results are complex, with many decisions that not only differ dramatically from *in vivo* imaging of small animals, but ultimately affect what questions can be answered using the data. This work represents “Part 2” of a 3-part series of recommendations and considerations for preclinical dMRI. We describe best practices for dMRI of *ex vivo* tissue, with a focus on the value that *ex vivo* imaging adds to the field of dMRI and considerations in *ex vivo* image acquisition. We first give general considerations and foundational knowledge that must be considered when designing experiments. We briefly describe differences in specimens and models and discuss why some may be more or less appropriate for different studies. We then give guidelines for *ex vivo* protocols, including tissue fixation, sample preparation, and MR scanning. In each section, we attempt to provide guidelines and recommendations, but also highlight areas for which no guidelines exist (and why), and where future work should lie. An overarching goal herein is to enhance the rigor and reproducibility of *ex vivo* dMRI acquisitions and analyses, and thereby advance biomedical knowledge.

Keywords: preclinical; diffusion MRI; *ex vivo*; best practices; microstructure; diffusion tensor; tractography; acquisition; processing; open science.

1 Introduction	5
2 Added Value	5
3 Ex vivo: Translation and validation considerations	7
3.1 Species differences	9
3.1.1 Murine models (mouse and rat)	10
3.1.2 Primate models	11
3.1.3 Human models	11
3.1.4 Other models	12
4 Acquisition	13
4.1 Standard Protocol - overview	13
4.2 Hardware (species/organ specific)	14
4.3 Fixation	14
4.4 Sample Preparation	17
4.5 MR Scanning	21
4.5.1 Encoding	21
4.5.2 Readout	22
4.5.3 q-t coverage	23
4.5.4 MR Scanning, Monitoring, scan duration	26
4.5.5 Spatial resolution	27
4.5.5.1 Volume equivalent resolutions and pushing the boundaries	27
4.6 Storage	29
5 Conclusions	29
6 Acknowledgements and Support	29
7 References	30

1 Introduction

Diffusion magnetic resonance imaging (dMRI) is a medical imaging technique that utilizes the diffusion of water molecules to generate image contrast, enabling the non-invasive mapping of the diffusion process in biological tissues. These diffusion patterns can be used to infer and generate maps of tissue microstructure, or can be applied to map tissue orientation to study the structural connections of the brain in a process called fiber tractography. They have found applications widely used in neuroscience, neuroanatomy, and neurology, but also outside the brain with musculoskeletal, whole-body, and organ-specific applications in normal and pathological conditions.

The use of animal models and *ex vivo* tissue is essential to the field of diffusion MRI. In this work, **we define *ex vivo* as covering any fresh excised tissue, perfused living tissue, or fixed tissue.** While dMRI enables non-invasive characterization of tissue *in vivo*, *ex vivo* dMRI acquisitions have several experimental advantages, including longer scanning times and absence of motion.

However, there are a number of considerations that must be made when performing *ex vivo* experiments. The steps from tissue preparation, image acquisition and processing, and interpretation of results are complex, with many decisions that not only differ dramatically from *in vivo* imaging of small animals, but ultimately affect what questions can be answered using the data. This work represents “Part 2” of a three-part series of recommendations and considerations for preclinical dMRI. Part 1 covers *in vivo* small animal imaging. Here Part 2 presents general considerations and best practices for preclinical dMRI acquisition of *ex vivo* tissue. Finally, Part 3 covers *ex vivo* data processing, tractography, and comparisons with histology. **This work does not serve as a “consensus” on any specific topic, but rather as a snapshot of “best practices” or “guidance”** from the preclinical dMRI community as represented by the authors. We envision this work to be useful to imaging centers using small animal scanners for research, sites that may not have personnel with expert knowledge in diffusion, pharmaceutical or industry employees, or new trainees in the field of dMRI. The resources provided herein may act as a starting point when reading the literature, and understanding the decisions and processes for studying model systems with dMRI.

We first describe the value that *ex vivo* imaging adds to the field of dMRI, followed by general considerations and foundational knowledge that must be considered when designing experiments. We briefly describe differences in specimens and models and discuss why some may be more or less appropriate for different studies. We then provide guidance for *ex vivo* acquisition protocols, including decisions on hardware, sample preparation, and imaging sequences. In each section, we attempt to also highlight areas for which no guidelines exist (and why), and where future work should lie. With this, we hope to enhance the rigor and reproducibility of *ex vivo* dMRI acquisitions and analyses, and thereby advance biomedical knowledge.

2 Added Value

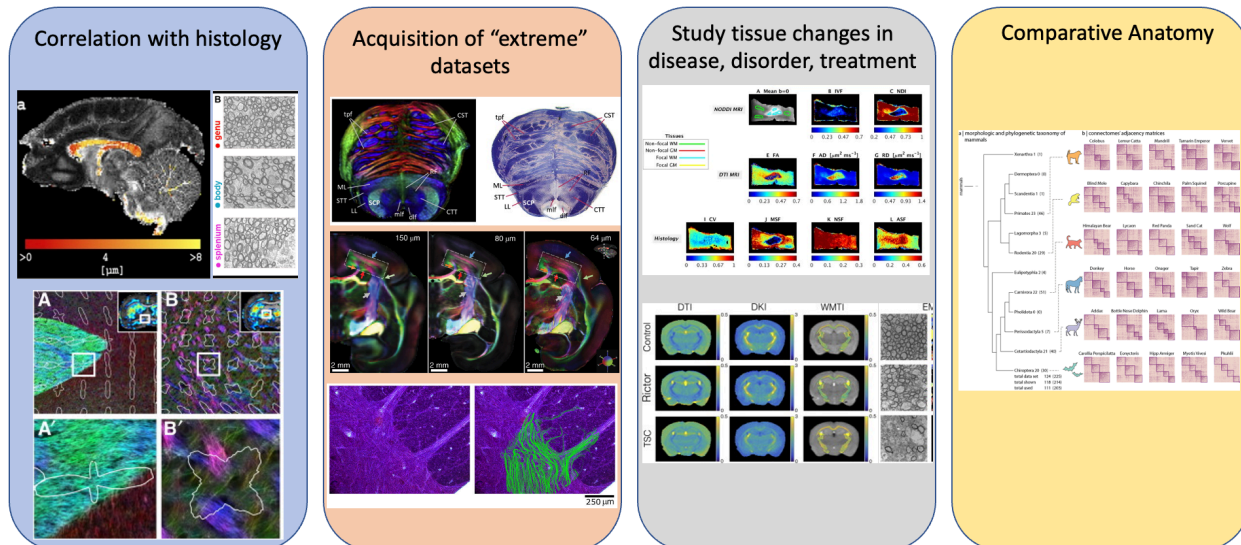


Figure 1. Four areas in which preclinical brain imaging adds value to the field of dMRI. It enables: (i) correlation with histology on the same subject/sample, (ii) the acquisition of richer datasets than on clinical systems thanks to more advanced hardware and longer scan times available, (iii) the study of tissue changes with disease and treatment in a more controlled setting, and (iv) comparative anatomy between species. Figures reused and adapted from (left to right): (i) ¹⁻³ (ii) ⁴⁻⁶ (iii) ^{7,8} (iv) ⁹.

Ex vivo samples add substantial value to dMRI by acting as supplements, substitutes, translations, and/or validation mechanisms for *in vivo* human studies. Building on the four areas identified in Part 1 in which preclinical MRI adds value to the field of diffusion MRI, here we focus on aspects specific to *ex vivo* experiments (**Figure 1**).

First, *ex vivo* dMRI allows correlations with histological and other imaging measures in a more direct way than *in vivo* dMRI, since the tissue has undergone the similar changes related to fixation and other chemical treatments. Through co-registration of microscopy images to MRI images of the same specimens, direct comparisons and correlation of dMRI measures to different quantitative microscopic parameters can be achieved, thus elucidating how different microscopic tissue features influence dMRI contrast. Such validation studies in turn improve our ability to interpret *in vivo* dMRI for both preclinical and clinical studies.

Second, *ex vivo* imaging allows acquisition of “extreme” datasets not possible with *in vivo* preclinical or clinical imaging, pushing the boundaries of acquisition and analysis to answer questions about what dMRI is capable of measuring in principle. By “extreme” datasets, we target in particular: advanced diffusion encoding, higher *b*-values, shorter diffusion times, or simply very comprehensive *q-t* coverage, all with high signal-to-noise ratio (SNR) and/or high spatial resolution that requires very long scan times. Preclinical MRI systems indeed offer four distinct advantages for imaging.

First, the appeal of **higher fields** is driven by benefits of potentially higher SNR due to increased net magnetization. Second, *ex vivo* imaging allows more flexibility in **RF coils**, which can be in close proximity to the sample being imaged, further increasing SNR. Third, **stronger and faster switching gradients** are also an immense asset for dMRI experiments¹⁰, enabling a higher SNR via reduced echo time. Stronger gradients facilitate the exploration of broader ranges of diffusion sensitization and diffusion time (i.e. “*q-t* space”) while keeping an acceptable SNR level. In particular, unique insights into tissue microstructure have been brought by exploring a range of *q-t* space only feasible (at the time) on preclinical systems^{11–15}, including very short diffusion times, very strong diffusion weightings^{11–14; 2,16,17}, or more complex diffusion encoding schemes^{18–20}. Finally, the greatest asset enabled by *ex vivo* imaging is a lengthy **scan time**, ranging from several hours to successful scans of >10 days in duration, with the added benefit of no physiological motion. Long scanning further facilitates acquisitions across *q-t* ranges, with substantially increased SNR and/or increased spatial resolution.

Third, the use of animal models allows us to study the sensitivity of dMRI to tissue changes in diseases, disorders and treatments in a controlled way. Animal models are critical to biomedical research as they may be biologically similar to humans, susceptible to many of the same health problems, and can be studied throughout their whole life span and across generations. *Ex vivo* imaging has the added benefit of bridging the gap between *in vivo* imaging and histology (Added Value #1) of such models, and investigation of new imaging sequences (Added Value #2) that together spur development and validation of new biomarkers for diagnosis and treatment.

Fourth, the use of *ex vivo* systems enables comparative anatomy. A key challenge in comparative neuroanatomy is to identify homologous structures and structural boundaries across species. Moreover, the brain undergoes substantial changes through development and aging which hampers comparison of data from different timepoints. High-resolution *ex vivo* structural MRI and dMRI data have provided versatile reference data for creating anatomical atlases for fly, mouse, rat, primate, and even bat brains^{21–28} allowing detection of detailed anatomical systems corresponding to those identified using histological criteria^{29,30}. Comparative neuroanatomical efforts, then, may rely on histological comparisons across species supplemented by high quality imaging acquisitions as a marker of ‘virtual histology’ and ‘virtual brain dissection’.

3 *Ex vivo*: Translation and validation considerations

Similar to *in vivo* studies of small animals, scanning *ex vivo* tissue presents both opportunities and challenges when translating and validating experimental findings³¹. This section introduces experimental and biological aspects that must be considered when designing and interpreting *ex vivo* studies. All aspects are covered in more detail in their corresponding sub-sections in *Acquisition* ([Section 4](#)).

Anatomical considerations

The basic constituents of the brain and other organs are largely preserved across mammalian species, providing the basis for translational MRI studies. Moreover, the constituents and organization of *ex vivo* tissue are largely similar to their *in vivo* counterparts, assuming appropriate perfusion fixation (to preserve ‘dead’ tissue) or artificial perfusion (to preserve ‘viable’ *ex vivo* tissue) ^{32,33}. For example, in the central nervous system, the fundamental structure of a long axon wrapped with a myelin sheath is preserved with chemical fixation *ex vivo*. Noticeable exceptions to similarity are possible changes in size, volume fractions of tissue compartments, membrane permeability and/or diffusivity drop beyond those that are expected from temperature changes (see *Considerations of microstructure and the diffusion process*, below) ^{34,35}.

Considerations in disease/disorder/model

As in small animal studies, a challenge when using *ex vivo* data to study the sensitivity of dMRI to detect changes in disease or treatments is confirming the translational value to human studies. Despite this, *ex vivo* imaging of models of stroke, demyelination, traumatic brain injury, spinal cord injury, and tumor models have proven useful to investigate altered microstructure or connectivity in diseased states, and facilitate subsequent histological validation ³⁶. Clearly, the advantage of small animal imaging for longitudinal studies of development or disease progression in single subjects stops at the *ex vivo* scan, yet the benefits of the high resolution and high SNR scan enable detailed investigations of the *ex vivo* tissue at one specific time point.

Considerations of microstructure and the diffusion process

The translation of *ex vivo* measurements to *in vivo* should be interpreted with caution, as both the tissue microstructure and intrinsic diffusivities may be different (**Figure 2**). To prevent postmortem degradation and to limit uncontrolled changes in tissue microstructure, tissues should be chemically fixed. Nevertheless, even using appropriate **chemical fixation**, the tissue inevitably undergoes changes: so far intra-/extracellular space volume fraction shifts, cell membrane permeability, relaxation rates and diffusion coefficients have all been shown to change ^{34,35,37–39}. The degree to which fixation affects microstructure features is however variable across the literature - see [Section 4.3](#) for details. *Ex vivo* dMRI on fixed tissue at room temperature also distinguishes itself through **lower diffusivity by a factor of 2-5** in the tissue, which cannot be explained by the difference in temperature alone, but is also due to fixation and/or other post-mortem tissue changes ⁴⁰. These effects should all be considered when designing the scanning protocol, and should be considered also when interpreting results in terms of diffusion distance and probed spatial scales ([Section 4.5.3](#)). Lastly, strategies for mitigating and/or correcting **temporal drift** are described throughout, and may involve sample preparation ([Section 4.4](#)), controlling temperature during scanning ([Section 4.5.4](#)) and within preprocessing pipelines (Part 3; Section 2).

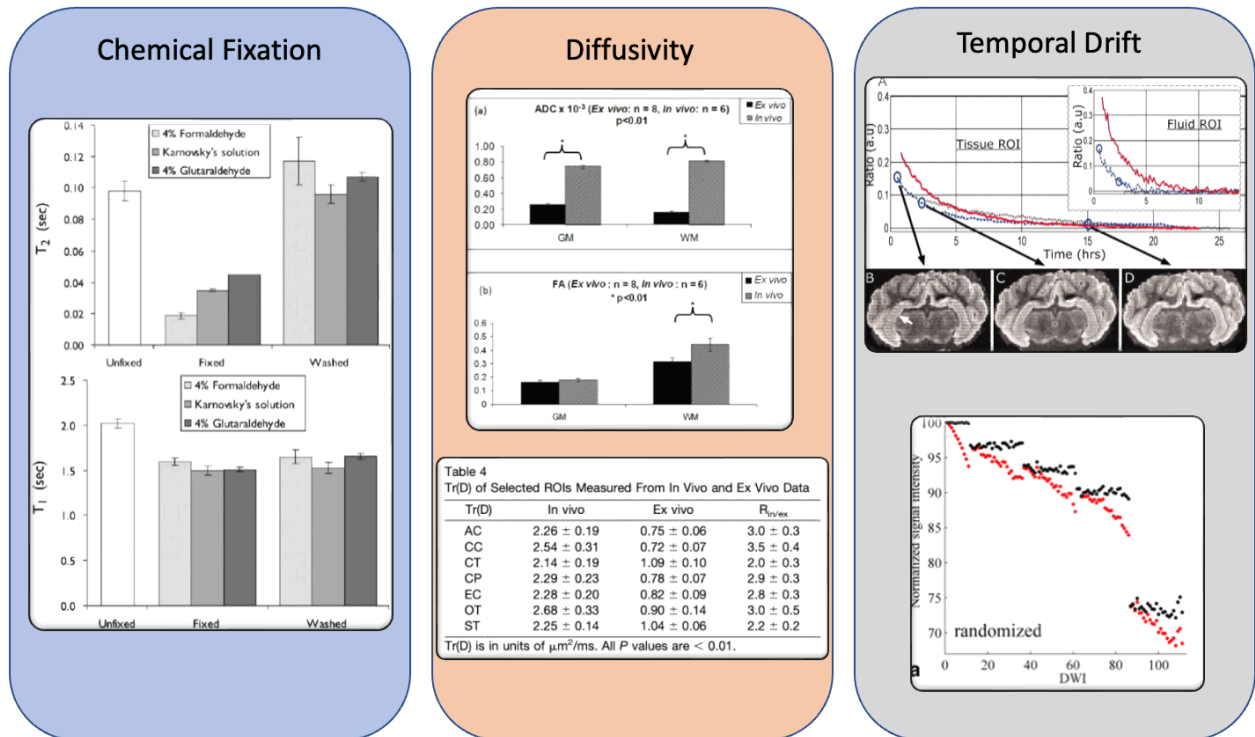


Figure 2 Considerations in the diffusion process. When performing studies on *ex vivo* tissue, one must consider effects of (i) chemical fixation (changes in geometry, volume fractions, relaxation rates, permeability, diffusion coefficients), (ii) changes in diffusivity (which can be ~2-5 times reduced from *in vivo* depending on experimental conditions), and (iii) temporal instabilities over long scan times (causing temporal drift or image artifacts). Figures reused and adapted from (i) ³⁵ (ii) ^{41,42} (iii) ^{43,44}

These effects need to be considered when interpreting *in vivo* dMRI based on *ex vivo* validation studies. A diffusion biophysical model that is validated or performs well *ex vivo* may not be valid/validated *in vivo*, and vice-versa, due to modeling assumptions, and potential differences in diffusivities, compartmental volume fractions, and relaxation rates.

3.1 Species differences

As discussed in Part 1, dMRI has been utilized in a number of animal models, both *in vivo* and *ex vivo*. The most appropriate species to investigate is ultimately dependent upon the research question. Of course, in studies of human anatomy, the postmortem human brain can also be imaged and subsequently dissected, or sectioned for histological analysis. Additionally improved SNR can be achieved and traded for spatial resolution by dissecting and imaging just the fragment of interest from the whole sample, thus allowing the use of smaller-bore, higher-magnetic field systems, and smaller RF coils.

Below, we list some of the most common species (and a few avantgarde ones) studied with *ex vivo* dMRI and briefly describe advantages and disadvantages of each.

3.1.1 Murine models (mouse and rat)

Rats and mice have been and continue to be the long-standing preferred species for biomedical research models as they offer a low-cost option with outcome measures widely available and a substantial database of normative data, including behavioral, genomic, and medical imaging (**Figure 3**). In addition to biological advantages, the small physical size offers technical advantages, fitting in the typically smaller bores (and smaller coils) of magnets with larger field strengths. This is particularly advantageous for *ex vivo* imaging, where the small size may facilitate scanning with smaller bore ultra-high field scanners and smaller volume coils or cryogenic probes. *Ex vivo*, mouse and rat models have found most applications in exploration and development of advanced image acquisition and diffusion encoding, and validation of multi-compartment modeling facilitated through subsequent histology.

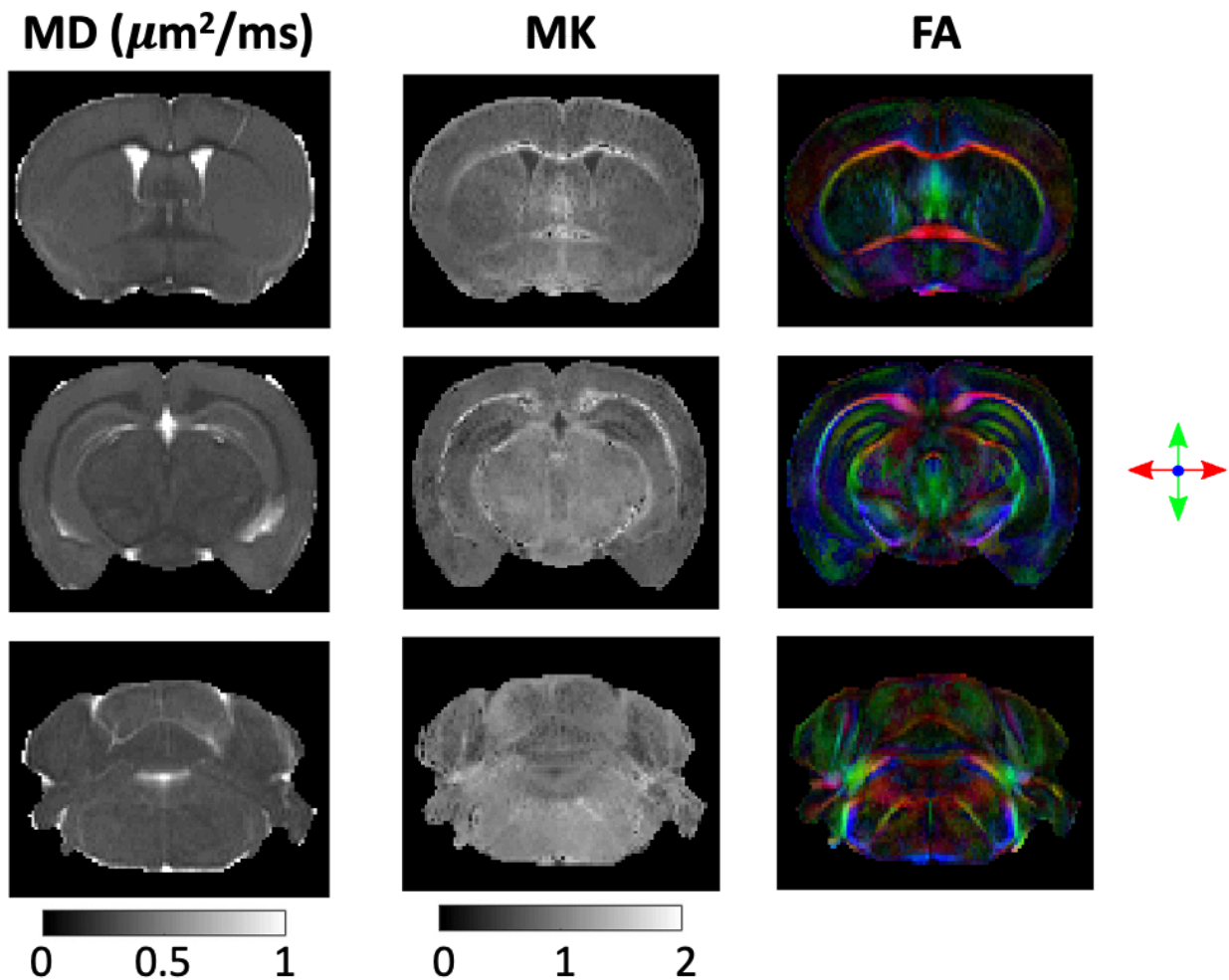


Figure 3. *Ex vivo* imaging of mouse models facilitates high resolution, high SNR, dense sampling of q - t space. Here, a fixed mouse brain was imaged on a 16.4T Bruker Aeon Ascend scanner equipped with a 10-mm birdcage coil and gradients capable of producing up to 3 T/m in all directions. Images show mean diffusivity (MD), Mean Kurtosis (MK), and directionally

encoded color (DEC) FA maps ⁴⁵. All animal studies were approved by the competent institutional and national authorities, and performed according to European Directive 2010/63. Images kindly provided by Andrada Ianus and Noam Shemesh.

3.1.2 Primate models

Popular non-human primates (NHPs) in dMRI literature include marmosets, squirrel monkeys, and macaques. With a number of white matter and gray matter regions with homologous counterparts in humans ^{46–49}, NHPs are well suited for studies of cortical development, gyrification, and the structural and functional significance of specific white matter pathways. *Ex vivo* NHP imaging, in particular, is very common after injection of histological tracers, and constitutes a majority of diffusion tractography validation studies (**Figure 4**). This enables comparisons of tracers to exceptional quality diffusion datasets, in order to identify challenges and limitations in diffusion tractography. For example, controversies regarding the existence or nonexistence of a pathway, or the location of pathway terminations have been resolved or steered through primate models ^{50–53}.

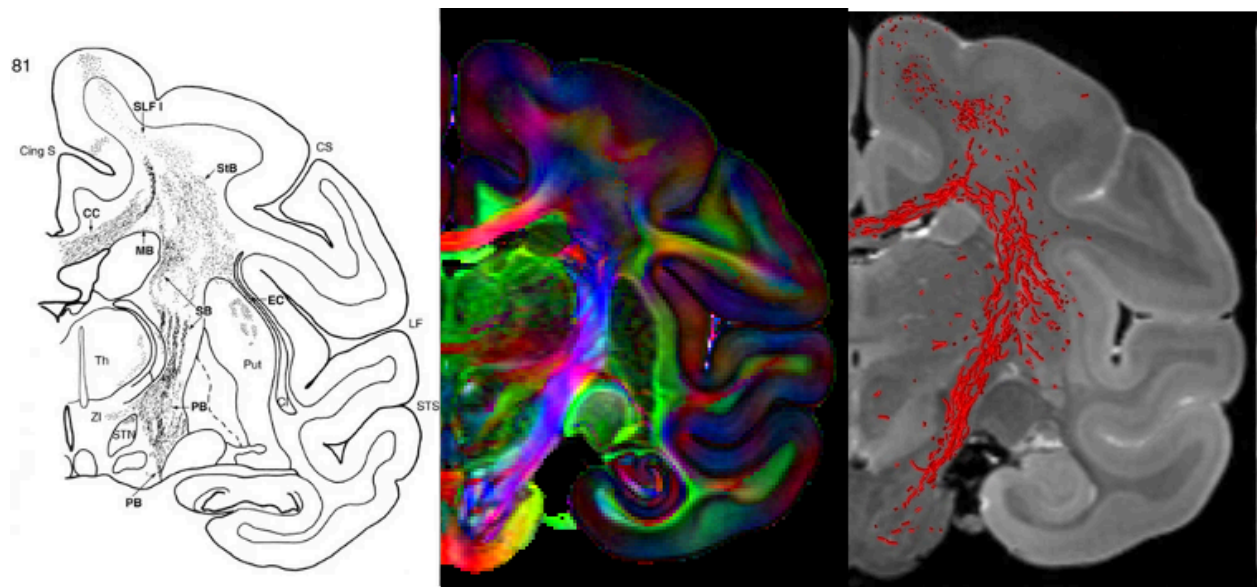


Figure 4. Primate models have been used to validate tractography estimates of structural connectivity. *Ex vivo* imaging offers the ability to investigate and compare the anatomical accuracy of high quality and high resolution dMRI datasets against histological tracers, the gold-standard for elucidating brain tractography. Figure adapted from ⁵⁴ and ⁵⁵, based on *ex vivo* macaque data acquired by ⁵⁶ shows tracer trajectory (left), directionally encoded color map (middle) and tractography streamlines (right).

3.1.3 Human models

Ex vivo imaging of human brains is also possible (**Figure 5**). Of course, the greatest advantage is the immediate translatability to the *in vivo* human brain. Because of the high resolution and rich (q-t) space coverage, *ex vivo* dMRI of the human brain has found a number

of neuroanatomical applications⁵⁷ including validation of orientation estimates and tractography^{58–61}, mapping of subcortical structures and creation of high resolution atlases and templates^{4,62,63}, and investigation of deep or cortical gray matter laminar structures^{43,64–66}. Challenges that are specific to human brain samples include limitations to medium-to-large bore systems (that often do not have specialized hardware such as strong gradient sets), and the need for specific sample holders or coils, although small sub-sections of human brains have also been scanned. Additionally, high quality scans are only possible on well-preserved samples, whereby minimizing the post-mortem interval between death and fixation is a necessity (see [Section 4.3 Fixation](#) for detailed discussion of the effects of post-mortem interval on MR-relevant tissue features).

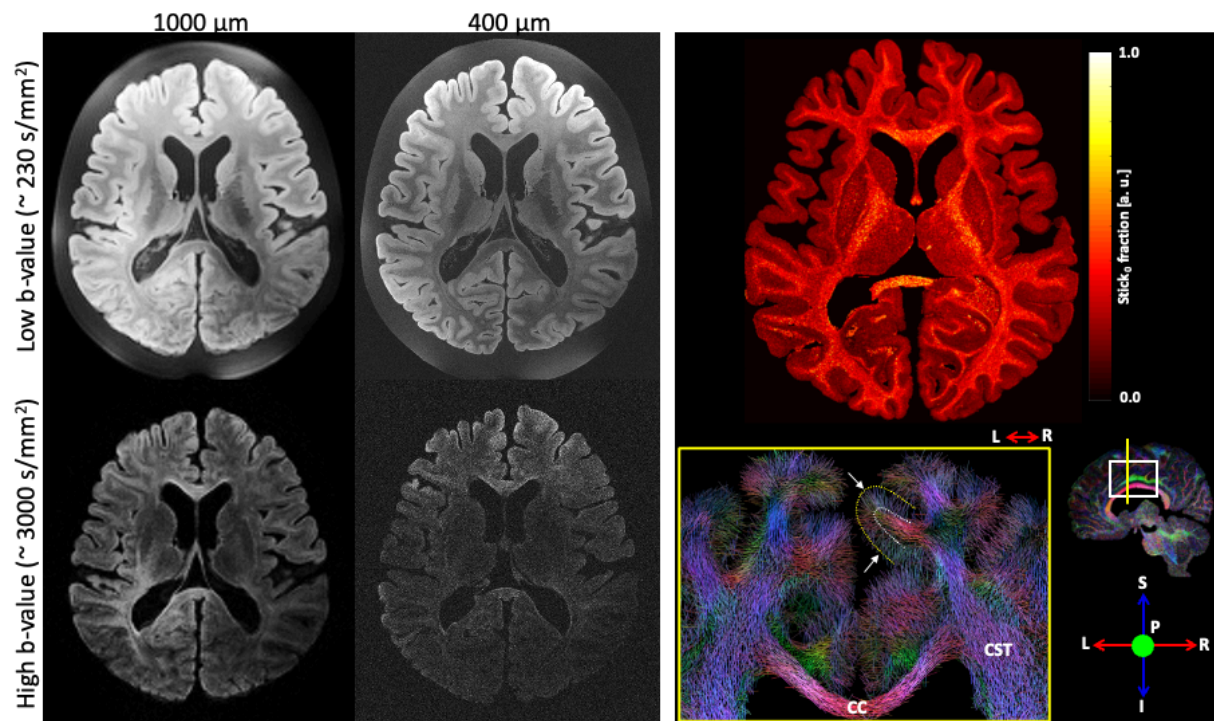


Figure 5. *Ex vivo* imaging of the human brain facilitates high resolution and high SNR dMRI (left), which offers exceptional tractography, mapping and creation of templates for small structures, and investigation of gray matter laminar structures (right). Images adapted from⁶⁷.

3.1.4 Other models

Several other models beyond murine and NHP have proven useful to the diffusion community. Examples include the pig brain, which has been used with *ex vivo* dMRI for tractography validation^{68–70}, and even to optimize strategies for *ex vivo* diffusion acquisitions⁴³. Other gyrencephalic brains have been used *ex vivo* to study diseases or to validate tractography include ferrets^{71–73}, sheep^{74–76}, dogs⁷⁷, and cats⁷⁸. One study scanned 123 mammalian species, with brains ranging in size from 0.1-1000mL, to study the evolution of mammalian brain connectivity⁷⁹.

Further, various non-human models of white matter, including cat optic nerves, rabbit peripheral nerves, garfish olfactory nerves, lobster nerves, and spinal cords were used to evaluate sources of anisotropy, and attribute and associate microstructural features to not only anisotropy, but restricted and hindered diffusion, compartmental diffusivities, and insight into pathology^{80,81}. Moreover, the simple nervous system with very large neurons of *Aplysia*, a sea slug, has been used to study the relationship between the cellular structure and the diffusion MRI signal, to characterize compartment-specific diffusion properties and to follow diffusion changes induced by neuronal responses to ischemic-like stress or chemical stimulation^{82–86}.

In general, dMRI studies of perfused viable tissue or cells present different advantages and/or challenges as compared to chemically fixed tissue. As mentioned above, isolated perfused ‘live’ tissue samples facilitate well controlled perturbation studies^{86,87}, for example controllably changing perfusate tonicity to induce cell swelling/shrinkage to model tissue alterations in stroke^{88,89}. Furthermore, the estimation of relative compartment sizes can also be thoroughly explored by controlling tonicity⁹⁰, especially since, without fixative, the tissue does not shrink.

4 Acquisition

4.1 Standard Protocol - overview

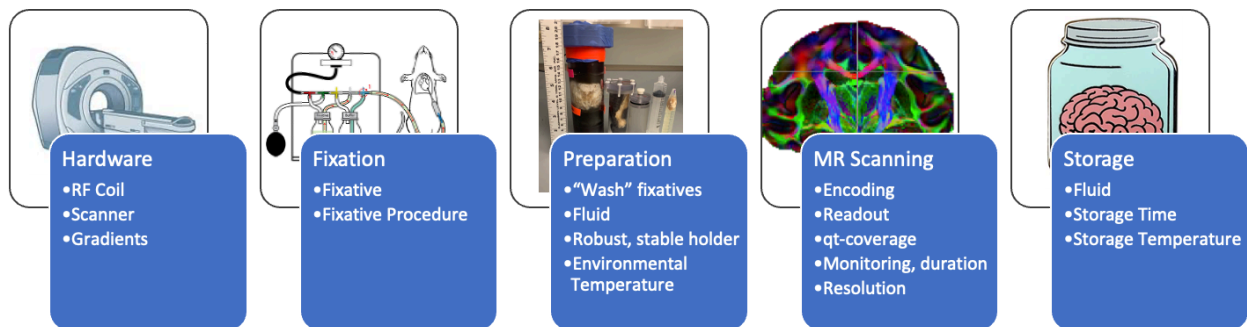


Figure 6. For high-quality *ex vivo* diffusion MRI, decisions regarding hardware, fixation, preparation, MR scanning, and tissue storage must be carefully considered. **Hardware:** utilize the smallest coil that fits the sample under investigation, to maximize SNR. **Fixation:** for *ex vivo* tissue to be a good model of *in vivo*, the post-mortem interval to fixation must be as short as possible. **Preparation:** washing out fixative and soaking tissue in a solution of Gadolinium-based contrast agent decreases primarily water-protons T_1 which in turn allows for a favorable trade-off between SNR maximization and TR reduction (i.e., reduced acquisition time), while a robust physical setup eliminates motion during scanning. **MR Scanning:** A multi-shot 3D diffusion-weighted spin echo EPI or multi-shot 3D diffusion-weighted RARE/FSE sequence. While not typically used *in vivo* due to motion sensitivity and long scan time, these sequences combine advantages of high SNR, minimal distortion, and reasonable scan time *ex vivo*. **Storage:** fixed tissue can be stored for many months to several years if stored in fixative or phosphate buffered solution (often with 1% PFA) at 5°C.

Here, we provide recommendations for (1) selecting appropriate hardware including MRI systems and coils ([Section 4.2](#)), (2) chemical fixation ([Section 4.3](#)), (3) sample preparation including washing, constraint and holders, possible contrast enhancements, and immersion solutions ([Section 4.4](#)), (4) MR scanning including diffusion encoding, readouts, q - t coverage, spatial resolution, and monitoring ([Section 4.5](#)), and (5) long term sample storage ([Section 4.6](#)).

4.2 Hardware (species/organ specific)

Most investigators are limited to the use of hardware available at their imaging center. The guidelines for *ex vivo* imaging largely follow those suggested for small animal imaging in Part 1 ⁹¹. **For RF Coils, the general recommendation is to utilize a coil that will maximize SNR for the sample of interest**, which will typically be the smallest coil that fits the sample under investigation. For *ex vivo* in particular, this is often a volume coil for both excitation and reception, as we typically desire (and have time for) covering the entire sample with the scan field of view, and volume coils have more homogeneous excitation/reception profiles than surface coils. Nevertheless, surface coils for reception can offer higher local SNR so the choice of coil setup depends on the imaging task.

If several MRI systems are available, a recommendation is to **select the scanner with the strongest and fastest gradients, highest field strength, that has a bore and appropriate coil that is large enough for the sample to be imaged**. Higher static magnetic field strengths provide higher SNR, but are challenged by changes in relaxation rates, for example increases in T_1 ⁹² and decreased T_2 ⁹³ (see *Sample Preparation* for discussion on techniques to alter both longitudinal and transverse relaxation, and see *Diffusion sequences: Readout* for discussion on taking advantage of altered relaxation rates).

4.3 Fixation

After death, tissues begin a self-degeneration process called autolysis, due to their own autogenous enzymes. This process degrades tissue quality, potentially altering several of the microstructural features we wish to quantify and/or validate against. Chemical fixation stops autolytic processes and preserves tissue structure by cross-linking proteins ⁹⁴. The postmortem interval (PMI) - i.e. the time between death and chemical fixation - is crucial for tissue quality. Anatomical and radiological signs of autolysis, such as myelin loosening, decreased anisotropy and decreased diffusivities, may be observed as rapidly as four to six hours postmortem, dependent upon tissue temperature, and continue to be altered with longer times between death and fixation ^{35,94,95}. Thus, rapid tissue fixation is recommended to maintain its integrity.

For laboratory animals, the method of choice is intracardiac **perfusion fixation**, which consists of using the intact vascular system to flush fixatives throughout the tissue upon animal sacrifice. This comes with the advantage of a mostly homogenized fixative distribution throughout the tissues and an efficient removal of blood by flushing with heparin-containing phosphate buffered saline (PBS) prior to perfusion with fixative.

For human tissues or in the case where perfusion-fixation is not possible for animals, perfusion fixation can sometimes be performed on post-mortem brain tissue using mechanical means^{57,96}.

Alternatively, tissue may be **immersion-fixed**, i.e. immersed in a fixative solution where fixative will passively diffuse throughout the tissue over a period of time (estimated at ~1 mm/hr at 25°C⁹⁴, or longer for refrigerated samples). For example, at least 20 days are needed for enough formaldehyde to diffuse to the core of a human brain to cause fixation (Dawe et al. 2009). Other tissue types may require different fixation durations, since the diffusion dynamics of the fixative solution are not the same as for the brain (e.g., 124 days for 4% formaldehyde to penetrate 30 mm into the whole human spleen, and 62 days for the fixative to diffuse over the same distance into mammalian liver tissue) (Dawe et al. 2009). As a major pitfall, immersion fixation introduces the risk of autolytic effects and microbial degradation⁹⁷ due to the PMI and/or delay in penetration of deep tissue in larger samples⁹⁸. As autolytic processes are temperature dependent, refrigerating the tissue as soon as possible after death, and during immersion fixation is recommended. Furthermore, this technique yields a transient concentration gradient of the fixative, and hence spatially inhomogeneous tissue integrity with varying MR characteristics (e.g., apparent T_1 and T_2). As a result, immersion fixed samples may exhibit lower anisotropy and diffusivity than their perfusion-fixed counterparts, in which case the differences may correlate with tissue degeneration. A rule of thumb to check the quality of fixed tissue (perfusion and immersion fixed) is that FA values should be the same as in vivo, e.g. as measured in the midsagittal corpus callosum. Nonetheless, immersion fixation holds the advantage of not relying on an intact vascular system, such that the most peripheral parts of the tissue can undergo good fixation even in the case of clogged blood vessels and/or trauma. Furthermore, perfusion-fixed tissues may additionally be post-fixed through the immersion process as well, often in a different concentration of the fixative.

In brief, we recommend minimizing the PMI to minimize autolytic changes in the tissue, refrigerating samples before and during immersion fixation and, whenever possible, sacrificing the animals using perfusion-fixation, which practically reduces the PMI to zero. For samples where perfusion fixation of the tissue is not possible (e.g. human brain samples) the recommendation is to keep PMI as constant as possible across samples and to state the PMI when reporting methods and results.

There are a number of fixatives to choose from, the most common being formaldehyde. For an overview of formaldehyde fixatives, see^{99,100}. Notably, the type and concentration of fixative can have a considerable impact on tissue relaxation properties^{35,95}, leading to differences in image SNR for dMRI. Neutral buffered formalin (NBF; formalin buffered with PBS) at 10% concentration can be used at room temperature and is most commonly used for immersion fixation in large samples (where higher temperature speeds up the penetration), while PFA at 4% in buffered solution should be kept cold and is standard for perfusion fixation. Both result in a 4% formaldehyde solution. Buffered fixatives (NBF or buffered PFA) may be preferred to their unbuffered versions. For example, brains fixed with NBF have higher T_2 values than brains fixed with standard formalin (¹⁰¹ - Figure 5). Reducing these fixative concentrations by half has been shown to also prolong T_2 and improve SNR in fixed tissue^{102,103}. The addition of glutaraldehyde to the fixative solution improves ultrastructural brain tissue preservation in the case of immersion-fixation¹⁰⁴, a mandatory requirement particularly for electron microscopy

cross-validation studies. The use of a fixative solution combining glutaraldehyde and paraformaldehyde has been shown to be MRI compatible while providing a better preservation of the cytoskeletal structures than paraformaldehyde fixative alone¹⁰⁵, while also better preserving membrane permeability³⁵. However, high glutaraldehyde concentrations can reduce the immunogenicity of antigens for immunohistochemistry analyses¹⁰⁰, but concentrations in the 0.05% range are acceptable¹⁰⁶. For an extensive discussion on other types of fixatives, as well as a comprehensive review on fixation in brain banking, see⁹⁷.

Even using the recommended procedures and concentrations for perfusion-fixation, there is discrepancy in the literature as to the degree of microstructural changes that the tissue undergoes. Studies mention for example variable levels of **preferential shrinkage** of certain compartments (e.g. the extracellular space)¹⁰⁷. Brains stored in formaldehyde-based fixatives may continually shrink during storage¹⁰⁸, with different structures experiencing differing rates of morphometric change and with different extents over time^{108,109}. It should be noted though that shrinkage due to chemical fixation is less than that during dehydration and tissue preparation for electron microscopy, for example^{32,94,107}. At the intracellular level, MR microscopy studies on immersion-fixed, isolated neurons from *Aplysia californica* show that formaldehyde affects nucleus and cytoplasm evenly⁸³. Notably, compartment models of diffusion *in vivo* have long yielded relative intra- to extracellular fractions of 30/70 (or 50/50 at best in white matter) which are in mismatch with 80/20 histological estimates of intra- vs extracellular compartment volume fractions^{110,111}. The latter are however more consistent with *ex vivo* diffusion models, which typically report 70/30 signal fractions¹¹². This suggests that *ex vivo* fixed tissue used for dMRI is closer to its histological counterpart than *in vivo* tissue. It is unclear though whether the change in relative dMRI compartment sizes between *in vivo* and *ex vivo* is due to non-uniform shrinkage with fixation or to non-uniform changes in compartment T_2 's, which affect the weighting of compartment signal contributions¹¹³. Methods such as cryo-fixation used for electron microscopy, which preserves the *in vivo* tissue compartment sizes more faithfully, could help shed light on some of these open questions^{107,114}.

Furthermore, there is still controversy as to whether chemical fixation increases or decreases **cell membrane permeability**^{38,115,116}, which is highly relevant for multi-compartment tissue models^{112,117}. A number of dMRI studies on fixed tissue have also reported an additional signal component in tissues, such as “isotropically-restricted water” in white matter (sometimes referred to as “still water” or “dot compartment”) that is not observed *in vivo*^{1,118,119} except for the cerebellum¹²⁰. This isotropically-restricted component is characterized by an extremely low diffusion coefficient, which gives rise to a non-vanishing diffusion-weighted signal even at high b -values (Alexander et al 2010). The exact origin of such a component is unknown, although it may be related to tissue overfixation or to vacuoles as visualized using synchrotron imaging¹²¹.

In addition, fixation alters the relaxation rates, substantially decreasing T_1 and T_2 ³⁵. The decrease in T_1 is understood to be due to the cross-linking of proteins that occurs in the fixation reaction, and is not reversible, whereas T_2 is decreased due to the presence of unbound fixative, and can be increased back closer to its *in vivo* value by washing³⁵. Consequently, tissue washing or rehydration is beneficial for SNR enhancement and must be considered when designing any *ex vivo* MRI acquisition protocol (see [Section 4.4](#)).

Finally, and crucially, fixation changes the water diffusion coefficient^{35,95,122,123}, with important implications for acquisition protocols and biophysical models of dMRI, as will be discussed in [Section 4.5.3](#).

4.4 Sample Preparation

Recommendations for sample preparation include (1) wash out free fixative, (2) ensure a robust mechanical setup to eliminate motion during scanning, and (3) verify temperature stabilization prior to acquiring data. If no tissue relaxometry or diffusion quantification is planned, (4) soaking in a Gadolinium-based solution might help to optimize the trade-off between SNR and acquisition time^{39,103}. We discuss each in detail below, and also consider the solution that samples may be scanned in.

First, prior to imaging fixed tissues that have been stored in the fixation fluid, **we recommend PBS ‘washes’ to rehydrate the sample and wash out free fixatives**. This simply entails placing the sample in a PBS solution, augmented with an antibacterial/antifungal product such as sodium azide, and replacing this PBS solution regularly. While the T_2 rises quickly, the washing time required for it to stabilize is dependent on sample size, geometry, volume and temperature of PBS solution, fixative concentration and previous time in fixative¹⁰³, with a wide variety of wash times noted in the literature (**Table 1**). To maximize T_2 and reduce the time to its stabilization, we recommend using as large a volume of PBS solution relative to the sample volume as practical, and replacing the solution more frequently in the first few hours/days/weeks of washing (e.g., every 12 – 72 hours), depending on sample size. To maximize tissue quality, we recommend refrigerating samples throughout the washing period. Of course, the larger human brain may require several weeks or more to fully wash.

Specimen	Approximate sample thickness	Soaking time	Fixative	PBS vol	Temperature	Number of solution changes	Reference
Ghost erythrocytes	80 μ l	12 hours	various	100 x sample vol		3	Thelwall et al., 2006, MRM
Rat cortical slices	0.5 mm	12 hours	4% formaldehyde		Room temperature	4-5	Shepherd et al., MRM, 2009; Shepherd et al., NI, 2009
Rat spinal cord	~2 mm	Overnight	4% formaldehyde				Shepherd et al., NI, 2009
Marmoset brain sections	2.5 mm	4 days	10% formaldehyde	10 x sample vol	4°C	0	D’Arceuil et al., 2007, NI
Marmoset brain	~ 20 mm	4-6 weeks	4% formaldehyde		4°C	0	Blezer et al., 2007, NMR Biomed
Rat brain in situ	~ 25 mm	\geq 20 days	2% formaldehyde	50 mL	4°C	0	Barrett et al., 2022
		\geq 47 days	4% formaldehyde	50 mL	4°C	0	Barrett et al., 2022
Macaque brain	~ 40 mm	\geq 25 days	10% formaldehyde	1 L	4°C	0	D’Arceuil et al., 2007, NI

		3 weeks	4% formaldehyde				Schilling et al., 2018, NI
Sheep brain	~ 50 mm	≥ 3 weeks	4% formaldehyde				Leprince et al., Proc ISMRM, 2015

Table 1. Examples of soaking times in PBS prior to MR imaging, depending on specimen size, fixative, etc.

To further increase SNR and CNR, gadolinium-based contrast agents are often added during the rehydration (washing) step. Gd is a paramagnetic contrast agent in the form of a chelate that facilitates longitudinal relaxation (reduces T_1), which allows TR minimization, particularly in 3D acquisition sequences, thus maximizing the SNR per unit time. Alternatively, Gd can be introduced during the perfusion step for small animals, in a technique referred to as ‘active staining’¹²⁴. If this is done, we still recommend immersing the sample in a Gd solution in addition. Typically, T_1 decreases are observed in the sample within 2-3 days in larger brains (macaque brain)³⁹, although we recommend soaking for 1-2 weeks in Gd solution depending on brain size. Naturally, a higher concentration of Gd results in shorter T_1 and T_2 ^{39,103}. The optimal concentration to use depends on acquisition timings (minimum TE, maximum TR) and on the method of staining (active staining typically uses a higher concentration than soaking), as well as field strength. Selected examples from the literature highlight the range of Gd contrasts and concentrations utilized with different acquisition choices given in **Table 2**.

Concentration (mM)	Contrast agent	TE (ms)	TR (ms)	Magnet (T)	Sample	Reference
1	Gd-DTPA	32	240	4.7	Macaque	D’Arceuil et al., 2007 ³⁹
1	Gd-DTPA	41	410	9.4	Squirrel Monkey	Schilling et al., 2019 ¹²⁵
0.5/0.5	Gd-DTPA	26	1000	9.4	Zebra Finch	Hamaide et al., 2016 ¹²⁶
5	Gadoteridol	11-15	125-150	11.7	Mouse	Tyszka et al., 2006; Tyszka & Frank, 2009 ¹²⁷
5/2.5	Gd-DTPA	21	100	7	Rat	Johnson et al., 2012 ¹²⁸
15/1	Gd-DTPA	27	250	9.4	Rat	Barrett et al., 2022 ¹⁰³
50/5	Gd-DTPA	15	100	9.4	Mouse	Calabrese et al., 2015 ¹²⁹

Table 2. Examples of the concentration of gadolinium contrast agent used in ex vivo dMRI studies from the literature. Where two concentration values are given, the first refers to the active staining concentration (contrast agent added in perfusion fixation), the second to passive staining (soaking post-fixation). A single concentration value refers to passive staining only.

As a caveat, the effects of gadolinium on specific tissue compartments are not well understood. T_1 longitudinal evaluation after Gd-doping exhibited a complex behavior of T_1 variation within different regions¹³⁰. Gd-soaking is thus best suited for tractography acquisitions, rather than quantitative dMRI studies. Gd staining to optimize SNR has been used without detrimental effects on histology or immunohistochemistry analysis^{103,131}.

Our second recommendation is to **ensure a robust mechanical setup to eliminate motion** during MRI data acquisition (**Figure 7**). The sample must be tightly constrained inside the imaging container, to prevent motion within the immersion fluid. This is critical to address both bulk motion and non-linear deformations that may arise over the duration of a long *ex vivo* scan (for example, bending of the brain stem). Notably, non-linear deformations are particularly challenging to correct when considering the importance of directional information in diffusion MRI. Sample-holders may be as simple as test tubes, or the cylinder of syringes (which may facilitate removal of air bubbles), as well as holders custom-made to fit within specific volume coils, often made with clear polycarbonate materials. In addition, some fluids that the sample is immersed in (see below) may have high densities, causing the sample to float if not properly constrained. Constraints are often applied through inserting foam pieces, where several groups have suggested very heavily reticulated foam to facilitate removal of air bubbles. Pieces of agar can also be used to stabilize tissue in a container, though agar is MR visible. If the above options are not feasible, post mortem brains can also be placed in a plastic bag. Here, the brain is wrapped with a thin layer of gaze in minimal fluid to reduce air bubbles and susceptibility effects, and the bag is slowly compressed until fluid is expelled to fully remove air bubbles, and tied tightly to ensure no leakage. Finally, very fragile tissue specimens, such as embryonic mouse brains, can be immersed in either agar gels, or kept within the skull, for increased mechanical support and to avoid deformation.

To minimize field inhomogeneities, ideally the holder will consist of a simple geometric shape (without sharp boundaries), with the sample immersed in a susceptibility matched fluid . The holder can be designed to minimize coil-to-sample distance, and to enable consistent sample positioning to eliminate any orientation effects and facilitate analysis.

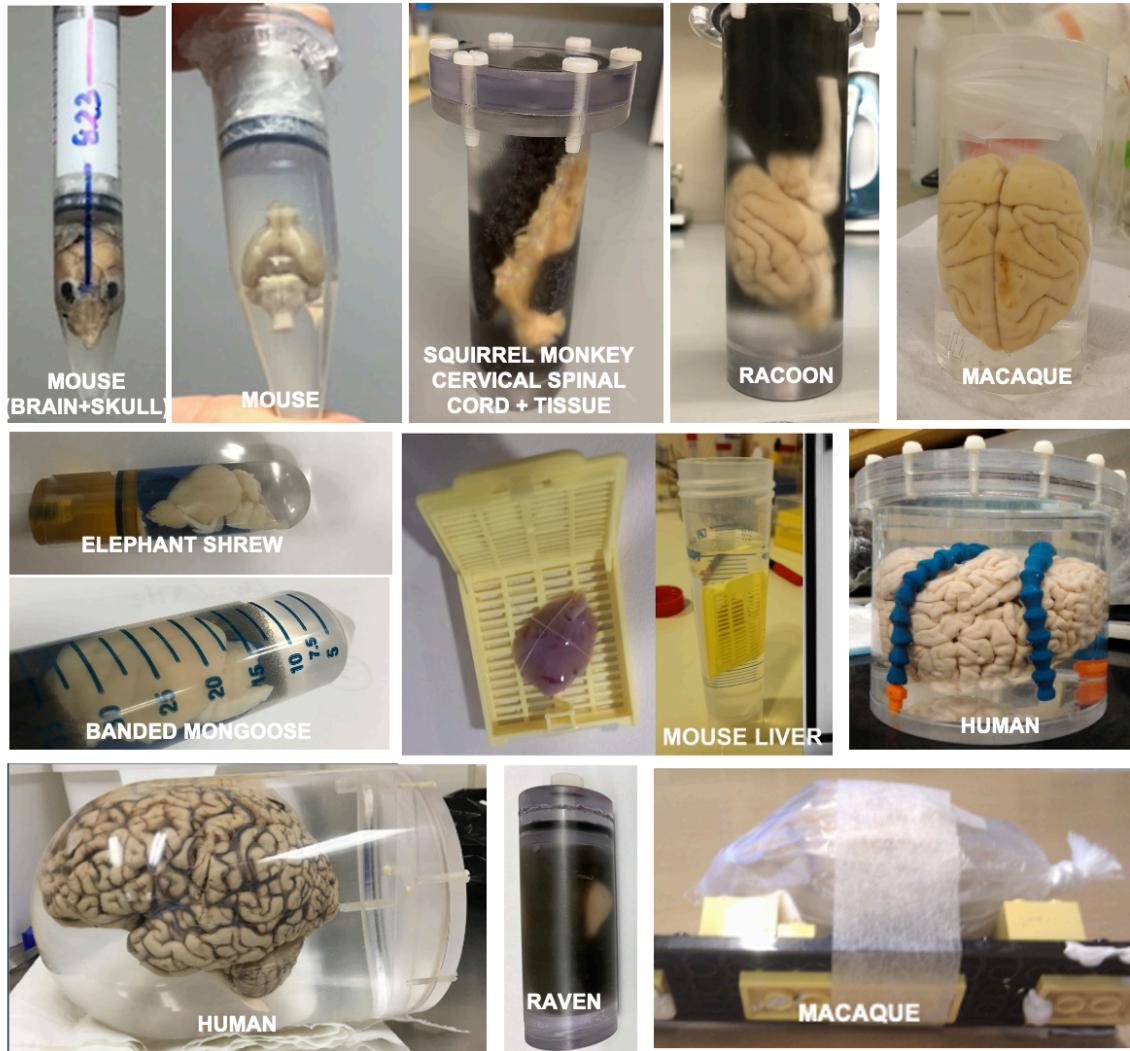


Figure 7. Examples of *ex vivo* samples prepared for dMRI acquisitions. Sample holders may be syringes or test tubes/falcon tubes, custom-made or 3D printed holders with ventilation valves, or simply placement within a plastic bag robustly secured to a platform. Photos courtesy of Daniel Colvin, Kurt Schilling, Luisa Ciobanu, Stijn Michielsse, Francesco Grussu, Raquel Perez-Lopez, Ileana Jelescu, Tim Dyrby.

Finally, recent advances allow 3D printing dedicated sample holders for minimizing motion/vibration, larger holders for human brains, and the ability to load multiple samples for simultaneous imaging (although with the disadvantage of requiring larger FOV, limited spatial resolution and sub-optimal shimming across samples).

For data acquisition, samples are typically immersed in either PBS or fluorinated oil. **In general, we suggest using a fluorinated oil, which are susceptibility-matched, inert compounds that do not have ^1H protons.** Thus, they lead to no signal in ^1H MR images, alleviating ghosting artifacts, facilitating image masking, and allowing a smaller, tighter FOV. A variety of fluorinated oils are suitable: perfluoropolyethers such as Fomblin (Solvay) or Galden (Solvay) or perfluorocarbons such as Fluorinert (3M), and can be recycled to be reused for multiple scans. While studies have not explicitly looked at the effects of these oils on

conventional or immuno-histology, it is our experience that they do not compromise nor interfere with this analysis¹³². However, it is recommended that after the MRI scan, excess oil be removed off the sample using absorbent paper, followed by several PBS washes to remove any residual oil in the cavities of the tissue sample. While these compounds are inert, the effect of long term storage of tissue in them is not known and thus not recommended.

Due to the strong difference in magnetic susceptibility with tissue, any air bubbles trapped in cavities such as brain sulci and ventricles will result in substantial image distortions and should be carefully removed during sample preparation by slightly turning, shaking and agitating the tissue. Alternatively, a vacuum setup to remove trapped air bubbles is very effective. Of note, due to the extremely low pressure, bubbles expand substantially, and the fluid can appear as 'boiling'. Lastly, a fine paintbrush may also be used to remove air bubbles while the sample is immersed.

Finally, to remove unwanted time-dependent signal contributions due to tissue temperature changing during scanning (from the cold storage to bore-temperature), **we advise placing the sample at the desired temperature for at least 4-8 hours prior to scanning**⁴³. It may be beneficial to run a dummy dMRI scan during these hours of temperature regularization to also stabilize possible temperature changes caused by gradient coil heating. As nonlinear motion of the tissue (due to physically handling and setting up the tissue in the magnet) is likely to occur immediately after handling, this extra waiting period (or dummy scans) may minimize motion during the scan itself. Timing should be kept consistent to avoid bias in group comparisons. During the scanning, the use of strong or varying diffusion weightings can influence the temperature environment of the tissue hence the diffusion coefficient. A constant airflow around the tissue can further stabilize the temperature.

4.5 MR Scanning

4.5.1 Encoding

Just as for *in vivo* small animal imaging (Part 1⁹¹), a number of possible **diffusion encoding**, or sensitization schemes are feasible, although the unique changes of decreased diffusivities and relaxation times must be considered. For *ex vivo* dMRI, the two most common encoding schemes are the **pulsed gradient spin echo (PGSE)**¹³³ and **steady-state free-precession (SSFP)** with diffusion preparation¹³⁴. For **PGSE** encoding, strong diffusion-sensitization gradients are applied on either side of a 180° refocusing pulse, resulting in a mathematically elegant way to describe diffusion weighting through the *b*-value, $b = (\gamma G \delta)^2 (\Delta - \delta/3)$, (where γ is the gyromagnetic ratio, G is the gradient strength, δ is the pulse duration, and Δ pulse separation). Because of its simplicity, PGSE is the most widespread diffusion weighting in both *in vivo* and *ex vivo* experiments.

Additionally, SSFP has been heavily utilized *ex vivo*. In **SSFP** acquisitions, the signal is retained over multiple repetition times, generating both spin echoes and stimulated echoes simultaneously. This results in both high SNR in the absence of diffusion gradients and in strong diffusion weighting in their presence. The primary advantage of SSFP is its highest SNR per unit time of all sequences, and its primary disadvantage is increased sensitivity to motion, limiting its use *in vivo*, but easily overcome *ex vivo*¹³⁴. However, unlike PGSE, the signal becomes a

complicated function of flip angle, TR, T_1 , T_2 , and the diffusion encoding, requiring specialized modeling to quantify diffusion coefficients¹³⁵.

Other encodings are also possible *ex vivo*, and described in more detail in Part 1. Briefly, **stimulated echo acquisition mode (STEAM)** sequences enable probing very long diffusion times with the disadvantage of half the SNR compared to PGSE (for equal echo times)⁶⁷.

Oscillating gradient spin echoes (OGSE) uses periodic sinusoidal gradients to probe much shorter times and length scales, which become particularly small with reduced diffusivity *ex vivo*, with limitations associated with attaining higher *b*-values^{136,137}. Finally, diffusion encoding can be applied along multiple spatial directions in **multi-dimensional diffusion encoding** experiments¹³⁸, which offers potential contrasts related to compartmental kurtosis, compartmental exchange, microscopic anisotropy, or heterogeneity of structural sizes/diameters.

4.5.2 Readout

For *ex vivo* imaging, readouts can be extremely diverse due to lack of sample motion and long available scan time. Our recommended starting protocol is a **multi-shot (segmented) 3D EPI sequence**. While this acquisition scheme comes at the cost of increased scan time and possible artifacts due to physiological motion *in vivo* vs. its 2D single shot counterpart, conveniently, *ex vivo* MRI is not limited by scan time nor motion, hence the recommendation. For this reason, it is not uncommon to use 4-12 segments, or more. The number of segments should ideally be chosen with the matrix size in mind so that segments of equal size are acquired.

Here, two features have been changed from the typical *in vivo* protocol: from single to multi-shot, and from 2D multi-slice to a 3D sequence. 3D EPI sequences are capable of achieving substantially higher SNR than 2D EPI^{41,139}. This SNR gain is due to averaging effects from Fourier encoding the entire tissue volume (i.e., collecting signal from the entire 3D tissue volume). SNR increases as the square root of the number of datapoints in the third spatial dimension, also referred to as second phase-encode direction, and which corresponds to the slice dimension in 2D multi-slice experiments¹⁴⁰. The rationale for going from single to multi-shot is that a strong segmentation of the 3D EPI read-out is necessary to prevent image distortions and prohibitively long echo times, especially if high spatial resolution is desired. 3D EPI also comes with the advantage of enabling acquisitions with truly isotropic resolution. Indeed, very high spatial resolutions in the third dimension may not be achievable in 2D multi-slice acquisitions, as very thin slices may not be feasible depending on the slice-selection gradient strength.

Despite the intrinsically higher SNR of 3D images, they suffer from suboptimal temporal utilization of T_1 relaxation. The TR with optimal SNR per unit time depends on the T_1 value of the tissue and can be determined by means of Bloch simulations or using the following

relationship: $SNR_t \sim M_0 \left(1 - e^{-TR/T_1}\right) e^{-TE/T_2}$. This equation can be used to determine the optimal TR in terms of **SNR efficiency** (SNR / $\sqrt{\text{(total imaging time)}}$):

$SNR_{efficiency} \sim (1/\sqrt{TR}) \left(1 - e^{-TR/T_1}\right)$. Conveniently, *ex vivo* imaging enables the addition of

Gadolinium-based contrast agents to the sample to shorten T_1 , and thus the optimal TR, facilitating high SNR efficiency. Example SNR efficiency curves are shown in **Figure 8**, where

the optimal TR is ~ 1.25 times the estimated T_1 (for examples of optimizing TE, TR, and diffusion weighting see *Other Considerations* in [Section 4.5.3 q-t coverage](#); for a discussion of advantages and limitations of contrast agents, see *Sample Preparation* [Section 4.4](#)). It should be noted however that short TR's may introduce T_1 weighting and affect the relative contributions of different compartments to the overall signal, in a similar manner to T_2 weighting.

Alternative readouts are also possible *ex vivo*. This includes the **2D EPI** and **spiral** readouts as *in vivo* (described in detail in Part 1 ⁹¹), and many *ex vivo* studies have taken advantage of the multiple RF echo trains of **RARE/FSE**, or **GRASE**, which often offers a good trade-off between scan time and image quality with high SNR and immunity to distortions. At the extreme end of acquisition is a **line-scan** readout, which traverses a single line of k -space per excitation. While this offers excellent robustness to susceptibility artifacts, it has a low SNR efficiency and may require excessively long scan times, or a tradeoff between spatial and angular resolutions. B_0 drift may also become problematic when the scan time is on the order of several days, and should be corrected for. Acquisitions can for example be split into 2-3 hour blocks, with the frequency (and shim, potentially requiring a new B_0 map to be acquired) readjusted before each block. This also allows retrieving at least partial data in the event the scanner crashes during the long acquisition.

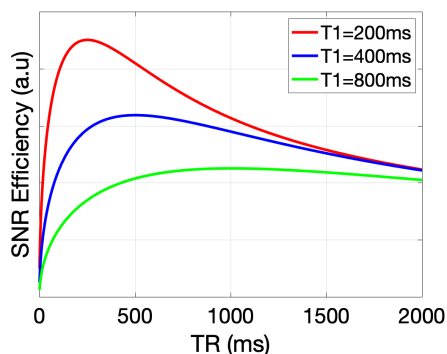


Figure 8. Plots showing how SNR efficiency varies with T_1 . Curves are based on the SNR-efficiency equation given in Section 4.5.2 based on a spin echo sequence. The optimal TR is ~ 1.25 times the sample T_1 , although there is a wide range of near-maximum efficiency. Similar optimization can be performed for TE, and diffusion weightings (see *Other Considerations* in [Section 4.5.3 q-t coverage](#) for examples)

4.5.3 q-t coverage

Before setting up diffusion parameters, it is important to understand the theoretical requirements of the chosen data analysis framework which will be used to process the data - this might include requirements of short gradient pulses, long/short diffusion times, certain b -value regimes, or a number of unique sampling directions.

The primary differences between *in vivo* (described in Part 1) and *ex vivo* data acquisition is the slower diffusion in fixed tissue, which often requires high b -value and/or longer diffusion times to ensure adequate signal attenuation and spin displacement: concretely, b -values should be adapted to ensure \sim constant bD product^{39,57} (we assume here that the sample has been washed to restore T_2 values, otherwise short T_2 is another consideration for fixed tissue). Indeed, *ex vivo* diffusivities of fixed tissue remain lower than *in vivo* even at 37°C,

the degree depending on the fixation method (perfusion-fixation or immersion) and postmortem interval^{35,39,43,57,141,142}. Moreover, scanning is often performed at room temperature, resulting in further reduction of diffusivity (change of -1–3% per °C). Selected examples are given in **Table 3**, where considerable decreases in diffusivity are observed across species in perfusion and immersion fixed brains, as well as in fresh *ex vivo* tissue. Notably, for tissue that has been suitably perfusion-fixed, the impact of fixation on the diffusivity is relatively comparable across samples/subjects.

	T1	T2	D	Specimen	Reference
Fixation (% change from in vivo to fixed)			↓ 80% ADC	macaque brain 2.5mm sections, immersion fixed	D'Arceuil et al., 2007, NI
			↓ 64% Trace	mouse brain perfusion fixed	Sun et al, 2003 MRM
			↓ 55% MD	Rat spinal cord perfused fixed	Madi et al, 2005, MRM
			↓ 72% Trace	mouse brain perfusion fixed	Sun et al, 2005, MRM
			↓ 50% MD	squirrel monkey, perfusion fixed	Schilling et al, 2017, MRI
			↓ 62% MD	rat brain, perfusion fixed	Wang et al., Eur Radiol Exp, 2018
	↓ 22%	↓ 5%	↓ 48% MD	Marmoset brain, immersion	Haga et al., Magn Res Med Sci, 2019
	↓ 40%	↓ 3%		mouse brain perfusion fixed	Guilfoyle et al, 2003, NMR Biomed
	↓ 63%	↓ 35%		human immersion fixed	Pfefferbaum et al, 2004, NI
	↓ 69%	↓ 27%		human immersion fixed	Birkel et al, 2016, NMR Biomed
Ex vivo fresh (% change from in vivo to ex vivo)			↓ 65-88% MD, AD, RD	fresh pig brain	Walker et al, 2019, PLoS One
			↓ 50% ADC	fresh monkey brain	D'Arceuil et al., 2007, NI
PBS washing (% change from fixed to washed)	↑ 7%	↑ 30%	↑ 30% ADC	macaque brain 2.5mm sections, immersion fixed	D'Arceuil et al., 2007, NI
	↑ 7%	↑ 3%	↑ 11% MD	human immersion fixed	Leprince et al, 2015, Proc ISMRM
	↑ 3%	↑ 72%	↑ 2% MD	rat brain, perfusion fixed	Barrett et al n.d.
			Reported no difference	Cat spinal cord, immersion fixed	Pattany et al, 1997, AJNR
	Reported no difference	↑ 516% (cortex)		rat cortical slices, immersion fixed	Shepherd et al., 2009, MRM
	↓ 14%	↑ 24%		Marmoset brain	Blezer et al, 2007, NMR Biomed

Table 3. Changes in T_1 , T_2 and D reported in the literature due to fixation and washing in PBS. Data is included from samples fixed with 10% Formalin or 4% PFA, scanned at room temperature. Measurements from WM only are included, unless otherwise noted.

Thus, for both fresh *ex vivo* and fixed tissue the drop in diffusivity is typically on the order of ~2-5 at room temperature, which corresponds to increasing the b -value by a similar factor to match the attenuation expected from an *in vivo* dMRI protocol. For postmortem human samples, however, due to non-negligible post-mortem interval and an extended duration of immersion

fixation needed to preserve cell and tissue components, the diffusivity is often on the order of 85% lower than *in vivo*^{143,144}, also in agreement with animal studies with extended PMI⁹⁵. Consequently, going beyond DTI protocols, including DKI and other advanced dMRI methods is sometimes challenging on postmortem human tissue due to the prohibitively high *b*-values required. For DTI, an adjusted *b*-value to about 4000 s/mm²³⁹ has been shown to result in similar signal attenuation as for an *in vivo* *b*=1000 s/mm² scan, and provide the angular contrast needed to resolve crossing fibers for tractography⁴³. It should, however, be noted that the optimal *b*-value for post-mortem acquisitions is a function of tissue fixation and scanning temperature and should be evaluated for each experiment individually.

Because of changes in diffusivity, it is important to consider spatial scales that are being probed. As diffusivity drops, diffusion distances proportional to \sqrt{Dt} drop as well - unless the diffusion time is prolonged accordingly - which results in different interactions between water molecules and the microscopic features they are able to probe. This may be beneficial when interested in probing geometry on small scales and also extends the limit of the narrow pulse approximation validity¹. This is additionally important in MR microscopy, where the resolutions start to approach the diffusion length scales and a significant amount of water may diffuse out of the imaging voxels in the echo time such that the spatial resolution is no longer 'real'.

Below, we provide guidelines for common applications of ex vivo imaging: signal representations (DTI/DKI), tractography, and biophysical signals models.

Diffusion tensor imaging (DTI): as in *in vivo*, recommendations include 20-30 non-collinear directions to mitigate noise, and *b*-value chosen so that the product $bD \approx 1$ to maximize precision. Ex vivo, this results in a *b*-value of approximately 2500 - 5000 s/mm², depending on the drop in diffusivity values. For Diffusion Kurtosis Imaging (DKI) the radius of convergence of the cumulant expansion ex vivo translates into the highest *b*-value roughly double the optimal one for DTI^{8,12,145,146} with a recommended 20-30 directions per shell.

For **tractography**, ex vivo guidelines again follow closely those of both small animal (Part 1) and human scans *in vivo* - our recommended protocol includes acquiring 50-60 directions at a moderate-to-high *b*-value, where a greater diffusion weighting (particularly for ex vivo) leads to a higher angular contrast and ability to resolve complex fiber architectures - for example Dyrby et al.⁴³ found a *b*-value of ~4000 s/mm² to lead to consistent fiber reconstructions with a high angular contrast, although a much larger range of *b*-values has also been utilized ex vivo with high angular accuracy and subsequent accurate tractography^{59,147-150}.

Regarding **compartment modeling**, it is critical to consider the data requirements of the intended biophysical model, specifically as it relates to diffusion times and diffusion weightings. Similarly, if diffusion-relaxometry experiments are intended, altered T_1 and T_2 depending on fixation and subsequent washing must be considered.

Other practical considerations

A great benefit in ex vivo imaging is the ability to conduct multiple experiments on the same tissue. Because relaxation and diffusivity can vary dramatically based on sample preparation (rehydration time, fixative, fixative concentration, contrast agent concentration, etc.) we recommend informing acquisition settings by acquiring scans prior to the start of a new study and optimizing using methods described in the literature^{39,103}. For example, It is particularly

advantageous to measure T_1 , T_2 , and diffusivity throughout the sample, and **SNR efficiency** can be optimized and tuned for both 2D and 3D sequences through changes in TE, TR, and diffusion weightings (**Figure 9**).

Other practical suggestions, as described in detail in Part 1 and also apply to *ex vivo* scans are to: (1) use an optimally distributed set of diffusion-encoding directions that cover the full sampling sphere (2) randomize ordering of acquisition of DWI images, especially across b -values to reduce or enable correction of temporal biases, reduce duty cycle, and allow analysis on partial acquisitions (3) intersperse several/many $b=0$ images throughout the scan to enable controlling for temporal drifts ⁴⁴, (4) use the effective b -matrix (i.e., the realized b -matrix taking into account other sequence gradients — rather than the nominal value entered into the scanner) which can be measured and validated in phantoms ¹⁵¹, and (5) perform high order shimming which may be critical for image quality, particularly at high field strengths due to their increased inhomogeneities.

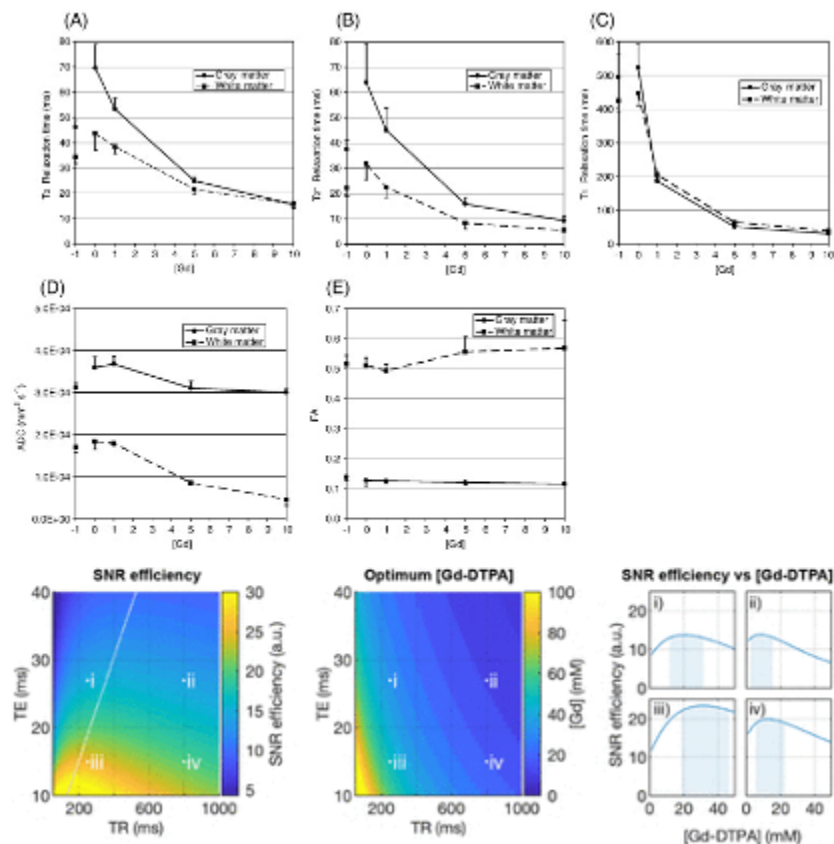


Figure 9. Approach to optimizing *ex vivo* diffusion protocols. Relaxometry (top) and diffusion (middle) can be measured as a function of contrast concentration, or fixative solution, for both white and gray matter tissue types, and SNR efficiency can be optimized (bottom) by manipulating sequence parameters and gadolinium contrast agent concentration. Images are adapted and modified from ³⁹ (top) and ¹⁰³ (bottom).

4.5.4 MR Scanning, Monitoring, scan duration

During long *ex vivo* scanning, it is important to minimize artifacts using several acquisition strategies. First, it is recommended that each image or volume be collected within as

short a time period as possible, i.e., inner-most loops should cover k-space sampling while outer-most loops should cover q-space sampling. Furthermore, if more than a single acquisition is performed using averaging, it is preferred to acquire each image separately split into repetitions, while saving the complex-valued data. Averaging repetitions in complex space rather than magnitude space is beneficial for lowering the noise floor to its theoretical zero-value, as opposed to being affected by the Rician noise floor; however, the advantage of initially saving these volumes as individual repetitions gives the opportunity to omit potentially corrupted individual images, if needed. Phase corrections prior to averaging are mandatory, and may need to be implemented by the user if not addressed well by the scanner reconstruction directly^{152,153}.

A stable temperature throughout the protocol is warranted to limit undesired signal drift due to T_1 -weighting and diffusivity variations. Potential sample temperature changes over time should therefore be prevented for example by ensuring an air flow around the tissue with constant temperature, as it is not easy to compensate for temperature drift in the post-processing pipeline. As a temperature control, a water vial can be placed next to the tissue and monitor its diffusivity over time, although it is important to carefully consider where the vial will appear within the field of view due to the addition of possible susceptibility, ringing, or ghosting artifacts. Of note, a temperature increase may also occur *in vivo*, though the effect may be less pronounced thanks to active thermal regulation of the animal.

Collectively, these strategies do not prevent the artifacts, but make them more addressable with subsequent post-processing.

4.5.5 Spatial resolution

For *in vivo* human or small animal imaging, spatial resolution should be as high as permissible for the targeted SNR and available scan time. However, *ex vivo* scans require different considerations when choosing a spatial resolution, due to the substantially increased scan time. While signal drift and temperature stability issues may arise due to increased scan time, resolution can be pushed quite extensively, with recent protocols nearly pushing the boundaries where resolution limits are set by the diffusion process itself, e.g. below 10 micrometers¹⁵⁴.

In short, there is no single set of guidelines, or consensus, on image resolution for specific species, nor for specific experimental designs. Rather than providing specific recommendations for resolution, below we give typical volumes of brains, and compute what the equivalent voxel size (i.e, the **volume equivalent resolution**) would be given the ratio of volumes, and a 2-mm isotropic human brain scan, typical of *in vivo* studies (**Table 4**). Further, we give examples of *ex vivo* scans that are **pushing the boundaries of resolution** - we note that these are not always feasible at every imaging center, and are not for any specific tractographic or modeling purposes, but only to highlight high resolution scans that have been performed.

4.5.5.1 Volume equivalent resolutions and pushing the boundaries

Species	Brain Volume (mL)	Matching spatial resolution (isotropic)	Reported in literature (<i>ex vivo</i>)
Human	1200	2 mm	730- μm isotropic ($b=3000 \text{ s/mm}^2$, 64 directions, 4 days, 3D-EPI) ¹⁴¹ 940- μm isotropic ($b\sim 4500 \text{ s/mm}^2$, 54 directions, 1m15s per volume, repeated 10 times, DW-SSFP) ¹⁴⁴ 1000- μm isotropic ($b\sim 5175\text{-}8550 \text{ s/mm}^2$, 49-52 directions, DW-SSFP, 10-11 minutes per volume) ¹⁴³ 500- μm isotropic ($b\sim 1700\text{-}5000 \text{ s/mm}^2$, 120 directions, DW-SSFP, 45 minutes per volume) ¹⁵⁵ 100- μm isotropic (hippocampus) ($b=4000 \text{ s/mm}^2$, 12 directions, 63hr acquisition) ⁶⁶ 200- μm isotropic (brainstem+thalamus) ($b=4000 \text{ s/mm}^2$, 120 directions, 208hr acquisition) ⁶³ 400- μm isotropic ($b\sim 3000 \text{ s/mm}^2$, 2h23m/volume); 500- μm isotropic ($b\sim 2000/4000 \text{ s/mm}^2$, 53m/volume); 1000- μm isotropic ($b\sim 1000 \text{ s/mm}^2$, 23m/volume) - kT-dSTEAM ⁶⁷
Mouse	0.4	140 μm	25- μm isotropic ($b=4000 \text{ s/mm}^2$, 61 directions, 95h scan, 3D-SE) ¹⁵⁶ 43- μm isotropic ($b=4000 \text{ s/mm}^2$, 120 directions, 235h scan, 3D-SE) ¹²⁹ 100- μm isotropic ($b=2000/5000 \text{ s/mm}^2$, 60 directions, 12h scan, 3D-SE) ¹⁵⁷
Rat	0.6	160 μm	50- μm isotropic ($b=3000 \text{ s/mm}^2$, 61 directions, 289h scan, 3D-SE) ¹⁵⁸ 150- μm isotropic ($b=3000/6000 \text{ s/mm}^2$, 30/30 directions, 21h scan, 3D-DW-GRASE) ¹⁵⁹ 88- μm isotropic ($b=800 \text{ s/mm}^2$, 12 directions, 18h scan, 3D-SE) ²⁷ 78- μm isotropic ($b=1500 \text{ s/mm}^2$, 6 directions) ²⁵ ($b=4000 \text{ s/mm}^2$, 30 directions) ²⁵
Squirrel monkey	35	600 μm	300- μm isotropic ($b=3000/6000/9000/12000 \text{ s/mm}^2$, 100 directions each, 48hr scan, 3D-EPI) ¹⁴⁹
Mini-Pig	64	750 μm	500- μm isotropic ($b=4009 \text{ s/mm}^2$), 61 directions, 28 hrs, 2D-SE) ⁷⁰
Macaque	80	800 μm	390x540x520 μm ($b=1000 \text{ s/mm}^2$, 8 directions, 45hr scan, 3D multiple echo SE) ²⁶ 500-1000 μm isotropic ($b=1477 - 9500 \text{ s/mm}^2$, 20-180 directions, up to 19 days scan, 2D-SE) ^{17,160,161} 600- μm isotropic ($b=4000 \text{ s/mm}^2$, 60 directions, 2D-SE single echo) ¹⁶² 200- μm isotropic ($b=100\text{-}10,000 \text{ s/mm}^2$, 3-36 directions, 93hr scan, 3D-EPI) ^{139,162} 200- μm isotropic ($b=500, 1000, 4000, 10\ 000 \text{ s/mm}^2$, 8- 16-32-64 directions respectively, 73hr scan, 3D-EPI) ¹³⁰ 300- μm isotropic ($b=6000 \text{ s/mm}^2$, 101 directions, 3D-EPI) ¹²⁵ 250- μm isotropic ($b=4800 \text{ s/mm}^2$, 121 directions, 71hr scan, 3D-EPI) ⁵⁶ 600- μm isotropic ($b = 4000 \text{ s/mm}^2$, 128 gradient directions, DW-SE multi-slice) ¹⁶³ 1000- μm isotropic ($b = 4000, 7000 \text{ and } 10000 \text{ s/mm}^2$, 250-1000-1000 directions respectively + spherical tensor encoding, DW-SE multi-slice) ¹⁶³
Macaque	35	600 μm	80- μm isotropic ($b=2400 \text{ s/mm}^2$, 64 directions, 15 days 3D-EPI) ⁵

Table 4. Summary of brain volumes of various species, matching spatial resolutions to the typical one for human dMRI, and ranges of spatial resolutions reported in the literature, *ex vivo*. The references provided are not comprehensive.

MR microscopy is defined as MR imaging with a spatial resolution in the micrometer range, which makes it possible to even image individual cells. Indeed, with dedicated setups that allow sufficiently high SNR, MRI with a resolution of a few μm becomes feasible ^{83,164–167}. By

convention, MRI transforms to MR microscopy (MRM) when the voxel side lengths are less than 100 μm ¹⁶⁸. A number of effects and considerations are encountered in MR microscopy that must be considered with respect to hardware, sequences, diffusion dispersion, and data processing. For an introduction to MRM emphasizing practical aspects relevant to high magnetic fields see¹⁶⁹, a review in¹⁷⁰, and details of microscale nuclear magnetic resonance hardware in¹⁷¹.

4.6 Storage

Ex vivo offers the advantage that repeated scans of fixed brains can be performed, enabling longer scans, multiple sessions, and optimization of the sequences and contrasts over time. **Here, if tissue storage is necessary, we recommend storing the samples in either a PBS solution with Sodium Azide to inhibit bacterial and fungal growth, or in a weak fixative solution (1% formalin in PBS), at low temperature (4-5°C).** Long-term storage at room temperature is also possible in 4% formaldehyde, although it is associated with an increase in formic acid and methanol which may have a dehydrating effect, and a slow decline in T1 and T2 relaxation times^{172,173}. These effects can be mitigated by regularly refreshing the formaldehyde solution and by sufficient rehydration prior to scanning. Several studies have investigated the effects of storage time on diffusion metrics, and concluded that with appropriate care, tissue can be rescanned over several years with negligible variability in results^{43,174}. Once fixed, the tissue quality should be inspected periodically^{32,43} to ensure tissue integrity and absence of bacterial or fungal growth.

5 Conclusions

In this manuscript, we have provided an overview of best practices for *ex vivo* diffusion MRI, focusing on experimental design, sample preparation, and MR scanning. These steps are critical to ensure rigorous and reproducible data collection, and pave the way for subsequent data processing. As we move to the next part of this series, we will shift our focus to pre-processing, model-fitting (processing), tractography, and comparisons with microscopy. Together, these recommendations are given to facilitate high quality studies and interpretation of *ex vivo* dMRI data.

6 Acknowledgements and Support

The authors acknowledge financial support from: the National Institutes of Health (K01EB032898, R01AG057991, R01NS125020, R01EB017230, R01EB019980, R01EB031954, R01CA160620, R01NS109090), the National Institute of Biomedical Imaging and Bioengineering (R01EB031765, R56EB031765), the National Institute on Drug Abuse (P30DA048742), the Secretary of Universities and Research (Government of Catalonia) Beatriu de Pinós postdoctoral fellowship (2020 BP 00117), “la Caixa” Foundation Junior Leader fellowship (LCF/BQ/PR22/11920010), the Research Foundation Flanders (FWO: 12M3119N),

the Belgian Science Policy Prodex (Grant ISLRA 2009–1062), the μ NEURO Research Center of Excellence of the University of Antwerp, the Institutional research chair in Neuroinformatics (Sherbrooke, Canada), the NSERC Discovery Grant, the European Research Council Consolidator grant (101044180), the Canada Research Chair in Quantitative Magnetic Resonance Imaging [950-230815], the Canadian Institute of Health Research [CIHR FDN-143263], the Canada Foundation for Innovation [32454, 34824], the Fonds de Recherche du Québec - Santé [322736], the Natural Sciences and Engineering Research Council of Canada [RGPIN-2019-07244], the Canada First Research Excellence Fund (IVADO and TransMedTech), the Courtois NeuroMod project, the Quebec BioImaging Network [5886, 35450], the Mila - Tech Transfer Funding Program and the Swiss National Science Foundation (Eccellenza Fellowship PCEFP2_194260), the Wellcome Trust (202788/Z/16/A, 203139/Z/16/Z and 203139/A/16/Z).

7 References

1. Alexander DC, Hubbard PL, Hall MG, et al. Orientationally invariant indices of axon diameter and density from diffusion MRI. *Neuroimage*. 2010;52(4):1374-1389.
2. Sepehrband F, Alexander DC, Kurniawan ND, Reutens DC, Yang Z. Towards higher sensitivity and stability of axon diameter estimation with diffusion-weighted MRI. *NMR Biomed*. 2016;29(3):293-308.
3. Budde MD, Frank JA. Examining brain microstructure using structure tensor analysis of histological sections. *Neuroimage*. 2012;63(1):1-10.
4. Aggarwal M, Zhang J, Pletnikova O, Crain B, Troncoso J, Mori S. Feasibility of creating a high-resolution 3D diffusion tensor imaging based atlas of the human brainstem: a case study at 11.7 T. *Neuroimage*. 2013;74:117-127.
5. Liu C, Ye FQ, Newman JD, et al. A resource for the detailed 3D mapping of white matter pathways in the marmoset brain. *Nat Neurosci*. 2020;23(2):271-280.
6. Hansen B, Flint JJ, Heon-Lee C, et al. Diffusion tensor microscopy in human nervous tissue with quantitative correlation based on direct histological comparison. *Neuroimage*. 2011;57(4):1458-1465.
7. Grussu F, Schneider T, Zhang H, Alexander DC, Wheeler-Kingshott CAM. Neurite orientation dispersion and density imaging of the healthy cervical spinal cord in vivo. *Neuroimage*. 2015;111:590-601.
8. Kelm ND, West KL, Carson RP, Gochberg DF, Ess KC, Does MD. Evaluation of diffusion kurtosis imaging in ex vivo hypomyelinated mouse brains. *Neuroimage*. 2016;124(Pt A):612-626.
9. Suárez LE, Yovel Y, van den Heuvel MP, et al. A connectomics-based taxonomy of mammals. doi:10.1101/2022.03.11.483995
10. Jones DK, Alexander DC, Bowtell R, et al. Microstructural imaging of the human brain with

- a “super-scanner”: 10 key advantages of ultra-strong gradients for diffusion MRI. *Neuroimage*. 2018;182:8-38.
11. Does MD, Parsons EC, Gore JC. Oscillating gradient measurements of water diffusion in normal and globally ischemic rat brain. *Magn Reson Med*. 2003;49(2):206-215.
 12. Aggarwal M, Smith MD, Calabresi PA. Diffusion-time dependence of diffusional kurtosis in the mouse brain. *Magn Reson Med*. 2020;84(3):1564-1578.
 13. Pyatigorskaya N, Le Bihan D, Reynaud O, Ciobanu L. Relationship between the diffusion time and the diffusion MRI signal observed at 17.2 Tesla in the healthy rat brain cortex. *Magn Reson Med*. 2014;72(2):492-500.
 14. Wu D, Martin LJ, Northington FJ, Zhang J. Oscillating gradient diffusion MRI reveals unique microstructural information in normal and hypoxia-ischemia injured mouse brains. *Magn Reson Med*. 2014;72(5):1366-1374.
 15. Assaf Y, Blumenfeld-Katzir T, Yovel Y, Basser PJ. AxCaliber: a method for measuring axon diameter distribution from diffusion MRI. *Magn Reson Med*. 2008;59(6):1347-1354.
 16. Jespersen SN, Bjarkam CR, Nyengaard JR, et al. Neurite density from magnetic resonance diffusion measurements at ultrahigh field: comparison with light microscopy and electron microscopy. *Neuroimage*. 2010;49(1):205-216.
 17. Dyrby TB, Sogaard LV, Hall MG, Ptito M, Alexander DC. Contrast and stability of the axon diameter index from microstructure imaging with diffusion MRI. *Magn Reson Med*. 2013;70(3):711-721.
 18. Xu J, Li H, Harkins KD, et al. Mapping mean axon diameter and axonal volume fraction by MRI using temporal diffusion spectroscopy. *Neuroimage*. 2014;103:10-19.
 19. Ianuş A, Jespersen SN, Serradas Duarte T, Alexander DC, Drobnyak I, Shemesh N. Accurate estimation of microscopic diffusion anisotropy and its time dependence in the mouse brain. *Neuroimage*. 2018;183:934-949.
 20. Lundell H, Nilsson M, Dyrby TB, et al. Multidimensional diffusion MRI with spectrally modulated gradients reveals unprecedented microstructural detail. *Sci Rep*. 2019;9(1):9026.
 21. Johnson GA, Badea A, Brandenburg J, et al. Waxholm space: an image-based reference for coordinating mouse brain research. *Neuroimage*. 2010;53(2):365-372.
 22. Aggarwal M, Zhang J, Mori S. Magnetic resonance imaging-based mouse brain atlas and its applications. *Methods Mol Biol*. 2011;711:251-270.
 23. Ullmann JFP, Watson C, Janke AL, Kurniawan ND, Reutens DC. A segmentation protocol and MRI atlas of the C57BL/6J mouse neocortex. *Neuroimage*. 2013;78:196-203.
 24. Liu C, Ye FQ, Yen CCC, et al. A digital 3D atlas of the marmoset brain based on multi-modal MRI. *Neuroimage*. 2018;169:106-116.
 25. Papp EA, Leergaard TB, Calabrese E, Johnson GA, Bjaalie JG. Waxholm Space atlas of the Sprague Dawley rat brain. *Neuroimage*. 2014;97:374-386.

26. Feng L, Jeon T, Yu Q, et al. Population-averaged macaque brain atlas with high-resolution ex vivo DTI integrated into in vivo space. *Brain Struct Funct*. 2017;222(9):4131-4147.
27. Veraart J, Leergaard TB, Antonsen BT, et al. Population-averaged diffusion tensor imaging atlas of the Sprague Dawley rat brain. *Neuroimage*. 2011;58(4):975-983.
28. Lee CH, Blackband SJ, Fernandez-Funez P. Visualization of synaptic domains in the Drosophila brain by magnetic resonance microscopy at 10 micron isotropic resolution. *Sci Rep*. 2015;5(1):8920.
29. Kjonigsen LJ, Lillehaug S, Bjaalie JG, Witter MP, Leergaard TB. Waxholm Space atlas of the rat brain hippocampal region: three-dimensional delineations based on magnetic resonance and diffusion tensor imaging. *Neuroimage*. 2015;108:441-449.
30. Osen KK, Imad J, Wennberg AE, Papp EA, Leergaard TB. Waxholm Space atlas of the rat brain auditory system: Three-dimensional delineations based on structural and diffusion tensor magnetic resonance imaging. *Neuroimage*. 2019;199:38-56.
31. Johnson GA, Benveniste H, Black RD, Hedlund LW, Maronpot RR, Smith BR. Histology by magnetic resonance microscopy. *Magn Reson Q*. 1993;9(1):1-30.
32. Dyrby TB, Innocenti GM, Bech M, Lundell H. Validation strategies for the interpretation of microstructure imaging using diffusion MRI. *Neuroimage*. 2018;182:62-79.
33. Flint JJ, Menon K, Hansen B, Forder J, Blackband SJ. A Microperfusion and In-Bore Oxygenator System Designed for Magnetic Resonance Microscopy Studies on Living Tissue Explants. *Sci Rep*. 2015;5:18095.
34. Zhang J, Jones MV, McMahon MT, Mori S, Calabresi PA. In vivo and ex vivo diffusion tensor imaging of cuprizone-induced demyelination in the mouse corpus callosum. *Magnetic Resonance in Medicine*. 2012;67(3):750-759. doi:10.1002/mrm.23032
35. Shepherd TM, Thelwall PE, Stanisz GJ, Blackband SJ. Aldehyde fixative solutions alter the water relaxation and diffusion properties of nervous tissue. *Magn Reson Med*. 2009;62(1):26-34.
36. Budde, Song. Insights into diffusion tensor imaging from animal models of white matter pathology. *Diffusion MRI: Theory, Methods and Applications*.
37. Wehrl HF, Bezrukov I, Wiehr S, et al. Assessment of murine brain tissue shrinkage caused by different histological fixatives using magnetic resonance and computed tomography imaging. *Histol Histopathol*. 2015;30(5):601-613.
38. Thelwall PE, Shepherd TM, Stanisz GJ, Blackband SJ. Effects of temperature and aldehyde fixation on tissue water diffusion properties, studied in an erythrocyte ghost tissue model. *Magn Reson Med*. 2006;56(2):282-289.
39. D'Arceuil HE, Westmoreland S, de Crespigny AJ. An approach to high resolution diffusion tensor imaging in fixed primate brain. *Neuroimage*. 2007;35(2):553-565.
40. Sun SW, Neil JJ, Liang HF, et al. Formalin fixation alters water diffusion coefficient magnitude but not anisotropy in infarcted brain. *Magn Reson Med*. 2005;53(6):1447-1451.

41. Rane S, Duong TQ. [No title]. doi:10.2174/18744440001105010172
42. Sun SW, Neil JJ, Song SK. Relative indices of water diffusion anisotropy are equivalent in live and formalin-fixed mouse brains. *Magn Reson Med*. 2003;50(4):743-748.
43. Dyrby TB, Baaré WFC, Alexander DC, Jelsing J, Garde E, Søgaard LV. An ex vivo imaging pipeline for producing high-quality and high-resolution diffusion-weighted imaging datasets. *Hum Brain Mapp*. 2011;32(4):544-563.
44. Vos SB, Tax CMW, Luijten PR, Ourselin S, Leemans A, Froeling M. The importance of correcting for signal drift in diffusion MRI. *Magnetic Resonance in Medicine*. 2017;77(1):285-299. doi:10.1002/mrm.26124
45. Pajevic S, Pierpaoli C. Color schemes to represent the orientation of anisotropic tissues from diffusion tensor data: application to white matter fiber tract mapping in the human brain. *Magn Reson Med*. 2000;43(6):921.
46. Nonhuman Primates and Medical Research. 1973. doi:10.1016/c2013-0-10403-5
47. Sibal LR, Samson KJ. Nonhuman Primates: A Critical Role in Current Disease Research. *ILAR Journal*. 2001;42(2):74-84. doi:10.1093/ilar.42.2.74
48. *The Squirrel Monkey in Biomedical and Behavioral Research.*; 2000.
49. Royo J, Forkel SJ, Pouget P, Thiebaut de Schotten M. The squirrel monkey model in clinical neuroscience. *Neurosci Biobehav Rev*. 2021;128:152-164.
50. Sarubbo S, Petit L, De Benedictis A, Chioffi F, Ptito M, Dyrby TB. Uncovering the inferior fronto-occipital fascicle and its topological organization in non-human primates: the missing connection for language evolution. *Brain Struct Funct*. 2019;224(4):1553-1567.
51. Mandonnet E, Sarubbo S, Petit L. The Nomenclature of Human White Matter Association Pathways: Proposal for a Systematic Taxonomic Anatomical Classification. *Front Neuroanat*. 2018;12:94.
52. Panesar SS, Fernandez-Miranda J. Commentary: The Nomenclature of Human White Matter Association Pathways: Proposal for a Systematic Taxonomic Anatomical Classification. *Front Neuroanat*. 2019;13:61.
53. Schilling KG, Rheault F, Petit L, et al. Tractography dissection variability: What happens when 42 groups dissect 14 white matter bundles on the same dataset? *Neuroimage*. 2021;243:118502.
54. Schmahmann JD, Pandya D. *Fiber Pathways of the Brain*. OUP USA; 2009.
55. Schilling KG, Petit L, Rheault F, et al. Brain connections derived from diffusion MRI tractography can be highly anatomically accurate-if we know where white matter pathways start, where they end, and where they do not go. *Brain Struct Funct*. 2020;225(8):2387-2402.
56. Thomas C, Ye FQ, Irfanoglu MO, et al. Anatomical accuracy of brain connections derived from diffusion MRI tractography is inherently limited. *Proc Natl Acad Sci U S A*. 2014;111(46):16574-16579.

57. Roebroek A, Miller KL, Aggarwal M. Ex vivo diffusion MRI of the human brain: Technical challenges and recent advances. *NMR Biomed.* 2019;32(4):e3941.
58. Budde MD, Annese J. Quantification of anisotropy and fiber orientation in human brain histological sections. *Front Integr Neurosci.* 2013;7:3.
59. Jones R, Grisot G, Augustinack J, et al. Insight into the fundamental trade-offs of diffusion MRI from polarization-sensitive optical coherence tomography in ex vivo human brain. *Neuroimage.* 2020;214:116704.
60. Roebroek A, Galuske R, Formisano E, et al. High-resolution diffusion tensor imaging and tractography of the human optic chiasm at 9.4 T. *Neuroimage.* 2008;39(1):157-168.
61. Seehaus A, Roebroek A, Bastiani M, et al. Histological validation of high-resolution DTI in human post mortem tissue. *Front Neuroanat.* 2015;9:98.
62. Adil SM, Calabrese E, Charalambous LT, et al. A high-resolution interactive atlas of the human brainstem using magnetic resonance imaging. *Neuroimage.* 2021;237:118135.
63. Calabrese E, Hickey P, Hulette C, et al. Postmortem diffusion MRI of the human brainstem and thalamus for deep brain stimulator electrode localization. *Hum Brain Mapp.* 2015;36(8):3167-3178.
64. Kleinnijenhuis M. *Imaging Fibres in the Brain.* Michiel Kleinnijenhuis; 2014.
65. Aggarwal M, Nauen DW, Troncoso JC, Mori S. Probing region-specific microstructure of human cortical areas using high angular and spatial resolution diffusion MRI. *Neuroimage.* 2015;105:198-207.
66. Ly M, Foley L, Manivannan A, Hitchens TK, Richardson RM, Modo M. Mesoscale diffusion magnetic resonance imaging of the ex vivo human hippocampus. *Hum Brain Mapp.* 2020;41(15):4200-4218.
67. Fritz FJ, Sengupta S, Harms RL, Tse DH, Poser BA, Roebroek A. Ultra-high resolution and multi-shell diffusion MRI of intact ex vivo human brains using k-dSTEAM at 9.4T. *Neuroimage.* 2019;202:116087.
68. Sauleau P, Lapouble E, Val-Laillet D, Malbert CH. The pig model in brain imaging and neurosurgery. *Animal.* 2009;3(8):1138-1151. doi:10.1017/s1751731109004649
69. Bech J, Orlowski D, Glud AN, Dyrby TB, Sørensen JCH, Bjarkam CR. Ex vivo diffusion-weighted MRI tractography of the Göttingen minipig limbic system. *Brain Struct Funct.* 2020;225(3):1055-1071.
70. Dyrby TB, Søgaard LV, Parker GJ, et al. Validation of in vitro probabilistic tractography. *Neuroimage.* 2007;37(4):1267-1277.
71. Hutchinson EB, Schwerin SC, Radomski KL, et al. Detection and Distinction of Mild Brain Injury Effects in a Ferret Model Using Diffusion Tensor MRI (DTI) and DTI-Driven Tensor-Based Morphometry (D-TBM). *Front Neurosci.* 2018;12:573.
72. Hutchinson EB, Schwerin SC, Radomski KL, Irfanoglu MO, Juliano SL, Pierpaoli CM. Quantitative MRI and DTI Abnormalities During the Acute Period Following CCI in the

- Ferret. *Shock*. 2016;46(3 Suppl 1):167-176.
73. Delettre C, Messé A, Dell LA, et al. Comparison between diffusion MRI tractography and histological tract-tracing of cortico-cortical structural connectivity in the ferret brain. *Netw Neurosci*. 2019;3(4):1038-1050.
 74. Looij Y van de, van de Looij Y, Lodygensky GA, et al. High-field diffusion tensor imaging characterization of cerebral white matter injury in lipopolysaccharide-exposed fetal sheep. *Pediatric Research*. 2012;72(3):285-292. doi:10.1038/pr.2012.72
 75. Pieri V, Trovatielli M, Cadioli M, et al. Diffusion Tensor Magnetic Resonance Tractography of the Sheep Brain: An Atlas of the Ovine White Matter Fiber Bundles. *Front Vet Sci*. 2019;6:345.
 76. Quezada S, van de Looij Y, Hale N, et al. Genetic and microstructural differences in the cortical plate of gyri and sulci during gyrification in fetal sheep. *Cereb Cortex*. 2020;30(12):6169-6190.
 77. Jacqmot O, Van Thielen B, Fierens Y, et al. Diffusion tensor imaging of white matter tracts in the dog brain. *Anat Rec* . 2013;296(2):340-349.
 78. Takahashi E, Dai G, Rosen GD, et al. Developing neocortex organization and connectivity in cats revealed by direct correlation of diffusion tractography and histology. *Cereb Cortex*. 2011;21(1):200-211.
 79. Assaf Y, Bouznach A, Zomet O, Marom A, Yovel Y. Conservation of brain connectivity and wiring across the mammalian class. *Nat Neurosci*. 2020;23(7):805-808.
 80. Beaulieu C. The basis of anisotropic water diffusion in the nervous system - a technical review. *NMR in Biomedicine*. 2002;15(7-8):435-455. doi:10.1002/nbm.782
 81. Beaulieu C, Allen PS. Water diffusion in the giant axon of the squid: implications for diffusion-weighted MRI of the nervous system. *Magn Reson Med*. 1994;32(5):579-583.
 82. Jelescu IO, Ciobanu L, Geffroy F, Marquet P, Le Bihan D. Effects of hypotonic stress and ouabain on the apparent diffusion coefficient of water at cellular and tissue levels in Aplysia. *NMR Biomed*. 2014;27(3):280-290.
 83. Lee CH, Flint JJ, Hansen B, Blackband SJ. Investigation of the subcellular architecture of L7 neurons of Aplysia californica using magnetic resonance microscopy (MRM) at 7.8 microns. *Sci Rep*. 2015;5:11147.
 84. Hsu EW, Aiken NR, Blackband SJ. A study of diffusion isotropy in single neurons by using NMR microscopy. *Magn Reson Med*. 1997;37(4):624-627.
 85. Grant SC, Buckley DL, Gibbs S, Webb AG, Blackband SJ. MR microscopy of multicomponent diffusion in single neurons. *Magn Reson Med*. 2001;46(6):1107-1112.
 86. Flint JJ, Menon K, Hansen B, Forder J, Blackband SJ. Visualization of live, mammalian neurons during Kainate-infusion using magnetic resonance microscopy. *Neuroimage*. 2020;219:116997.
 87. Flint J, Hansen B, Vestergaard-Poulsen P, Blackband SJ. Diffusion weighted magnetic

- resonance imaging of neuronal activity in the hippocampal slice model. *Neuroimage*. 2009;46(2):411-418.
88. Hsu EW, Aiken NR, Blackband SJ. Nuclear magnetic resonance microscopy of single neurons under hypotonic perturbation. *Am J Physiol*. 1996;271(6 Pt 1):C1895-C1900.
 89. Blackband SJ, Flint JJ, Hansen B, et al. On the Origins of Diffusion MRI Signal Changes in Stroke. *Front Neurol*. 2020;11. doi:10.3389/fneur.2020.00549
 90. Thelwall PE, Grant SC, Stanisz GJ, Blackband SJ. Human erythrocyte ghosts: exploring the origins of multiexponential water diffusion in a model biological tissue with magnetic resonance. *Magn Reson Med*. 2002;48(4):649-657.
 91. Jelescu IO, Grussu F, Ianus A, Hansen B. Recommendations and guidelines from the ISMRM Diffusion Study Group for preclinical diffusion MRI: Part 1--In vivo small-animal imaging. *arXiv preprint arXiv*. 2022. <https://arxiv.org/abs/2209.12994>.
 92. Rooney WD, Johnson G, Li X, et al. Magnetic field and tissue dependencies of human brain longitudinal $1\text{H}_2\text{O}$ relaxation in vivo. *Magn Reson Med*. 2007;57(2):308-318.
 93. de Graaf RA, Brown PB, McIntyre S, Nixon TW, Behar KL, Rothman DL. High magnetic field water and metabolite proton T1 and T2 relaxation in rat brain in vivo. *Magn Reson Med*. 2006;56(2):386-394.
 94. Fox CH, Johnson FB, Whiting J, Roller PP. Formaldehyde fixation. *J Histochem Cytochem*. 1985;33(8):845-853.
 95. D'Arceuil H, de Crespigny A. The effects of brain tissue decomposition on diffusion tensor imaging and tractography. *Neuroimage*. 2007;36(1):64-68.
 96. Grinberg LT, Amaro E Jr, Teipel S, et al. Assessment of factors that confound MRI and neuropathological correlation of human postmortem brain tissue. *Cell Tissue Bank*. 2008;9(3):195-203.
 97. McFadden WC, Walsh H, Richter F, et al. Perfusion fixation in brain banking: a systematic review. *Acta Neuropathol Commun*. 2019;7(1):146.
 98. Dawe RJ, Bennett DA, Schneider JA, Vasireddi SK, Arfanakis K. Postmortem MRI of human brain hemispheres: T2 relaxation times during formaldehyde fixation. *Magn Reson Med*. 2009;61(4):810-818.
 99. Vučković I, Nayfeh T, Mishra PK, et al. Influence of water based embedding media composition on the relaxation properties of fixed tissue. *Magn Reson Imaging*. 2020;67:7-17.
 100. Kiernan JA. Formaldehyde, formalin, paraformaldehyde and glutaraldehyde: What they are and what they do. *Micros Today*. 2000;8(1):8-13.
 101. Tendler BC, Qi F, Foxley S, et al. A method to remove the influence of fixative concentration on postmortem T2 maps using a kinetic tensor model. *Hum Brain Mapp*. 2021;42(18):5956-5972.
 102. Birkl C, Soellradl M, Toeglhofer AM, et al. Effects of concentration and vendor specific

- composition of formalin on postmortem MRI of the human brain. *Magn Reson Med*. 2018;79(2):1111-1115.
103. Barrett RLC, Cash D, Simmons C, et al. Tissue Optimisation Strategies for High Quality Ex Vivo Diffusion Imaging. doi:10.1101/2021.12.13.472113
 104. Morin F, Crevier C, Bouvier G, Lacaille JC, Beaulieu C. A fixation procedure for ultrastructural investigation of synaptic connections in resected human cortex. *Brain Res Bull*. 1997;44(2):205-210.
 105. Schwartz ED, Cooper ET, Chin CL, Wehrli S, Tessler A, Hackney DB. Ex vivo evaluation of ADC values within spinal cord white matter tracts. *AJNR Am J Neuroradiol*. 2005;26(2):390-397.
 106. Welikovich LA, Do Carmo S, Maglóczy Z, et al. Evidence of intraneuronal A β accumulation preceding tau pathology in the entorhinal cortex. *Acta Neuropathol*. 2018;136(6):901-917.
 107. Korogod N, Petersen CCH, Knott GW. Ultrastructural analysis of adult mouse neocortex comparing aldehyde perfusion with cryo fixation. *Elife*. 2015;4. doi:10.7554/eLife.05793
 108. de Guzman AE, Wong MD, Gleave JA, Nieman BJ. Variations in post-perfusion immersion fixation and storage alter MRI measurements of mouse brain morphometry. *Neuroimage*. 2016;142:687-695.
 109. Zhang J, Peng Q, Li Q, et al. Longitudinal characterization of brain atrophy of a Huntington's disease mouse model by automated morphological analyses of magnetic resonance images. *Neuroimage*. 2010;49(3):2340-2351.
 110. Clark CA, Le Bihan D. Water diffusion compartmentation and anisotropy at high b values in the human brain. *Magn Reson Med*. 2000;44(6):852-859.
 111. Jelescu IO, Zurek M, Winters KV, et al. In vivo quantification of demyelination and recovery using compartment-specific diffusion MRI metrics validated by electron microscopy. *Neuroimage*. 2016;132:104-114.
 112. Olesen JL, Østergaard L, Shemesh N, Jespersen SN. Diffusion time dependence, power-law scaling, and exchange in gray matter. *Neuroimage*. 2022;251:118976.
 113. Jelescu IO, Palombo M, Bagnato F, Schilling KG. Challenges for biophysical modeling of microstructure. *J Neurosci Methods*. 2020;344:108861.
 114. Pallotto M, Watkins PV, Fubara B, Singer JH, Briggman KL. Extracellular space preservation aids the connectomic analysis of neural circuits. *Elife*. 2015;4. doi:10.7554/eLife.08206
 115. Porea A, Webb AG. Reversible and irreversible effects of chemical fixation on the NMR properties of single cells. *Magn Reson Med*. 2006;56(4):927-931.
 116. Sønderby CK, Lundell HM, Sjøgaard LV, Dyrby TB. Apparent exchange rate imaging in anisotropic systems. *Magn Reson Med*. 2014;72(3):756-762.
 117. Jelescu IO, de Skowronski A, Geffroy F, Palombo M, Novikov DS. Neurite Exchange

- Imaging (NEXI): A minimal model of diffusion in gray matter with inter-compartment water exchange. *Neuroimage*. 2022;256:119277.
118. Panagiotaki E, Schneider T, Siow B, Hall MG, Lythgoe MF, Alexander DC. Compartment models of the diffusion MR signal in brain white matter: a taxonomy and comparison. *Neuroimage*. 2012;59(3):2241-2254.
 119. Grussu F, Schneider T, Tur C, et al. Neurite dispersion: a new marker of multiple sclerosis spinal cord pathology? *Ann Clin Transl Neurol*. 2017;4(9):663-679.
 120. Tax CMW, Szczepankiewicz F, Nilsson M, Jones DK. The dot-compartment revealed? Diffusion MRI with ultra-strong gradients and spherical tensor encoding in the living human brain. *Neuroimage*. 2020;210:116534.
 121. Andersson M, Kjer HM. Axon morphology is modulated by the local environment and impacts the noninvasive investigation of its structure–function relationship. *Proceedings of the*. 2020. <https://www.pnas.org/content/117/52/33649.short>.
 122. Lohr D, Terekhov M, Veit F, Schreiber LM. Longitudinal assessment of tissue properties and cardiac diffusion metrics of the ex vivo porcine heart at 7 T: Impact of continuous tissue fixation using formalin. *NMR Biomed*. 2020;33(7):e4298.
 123. Tovi M, Ericsson A. Measurements of T1 and T2 over time in formalin-fixed human whole-brain specimens. *Acta radiol*. 1992;33(5):400-404.
 124. Johnson GA, Cofer GP, Gewalt SL, Hedlund LW. Morphologic phenotyping with MR microscopy: the visible mouse. *Radiology*. 2002;222(3):789-793.
 125. Schilling K, Gao Y, Janve V, Stepniewska I, Landman BA, Anderson AW. Can increased spatial resolution solve the crossing fiber problem for diffusion MRI? *NMR Biomed*. 2017;30(12). doi:10.1002/nbm.3787
 126. Hamaide J, De Groof G, Van Steenkiste G, et al. Exploring sex differences in the adult zebra finch brain: In vivo diffusion tensor imaging and ex vivo super-resolution track density imaging. *Neuroimage*. 2017;146:789-803.
 127. Tyszka JM, Readhead C, Bearer EL, Pautler RG, Jacobs RE. Statistical diffusion tensor histology reveals regional dysmyelination effects in the shiverer mouse mutant. *Neuroimage*. 2006;29(4):1058-1065.
 128. Johnson GA, Calabrese E, Badea A, Paxinos G, Watson C. A multidimensional magnetic resonance histology atlas of the Wistar rat brain. *Neuroimage*. 2012;62(3):1848-1856.
 129. Calabrese E, Badea A, Cofer G, Qi Y, Johnson GA. A Diffusion MRI Tractography Connectome of the Mouse Brain and Comparison with Neuronal Tracer Data. *Cereb Cortex*. 2015;25(11):4628-4637.
 130. Sébille SB, Rolland AS, Welter ML, Bardinet E, Santin MD. Post mortem high resolution diffusion MRI for large specimen imaging at 11.7 T with 3D segmented echo-planar imaging. *J Neurosci Methods*. 2019;311:222-234.
 131. Spencer RG, Fishbein KW, Cheng A, Mattson MP. Compatibility of Gd-DTPA perfusion

- and histologic studies of the brain. *Magn Reson Imaging*. 2006;24(1):27-31.
132. Iglesias JE, Crampsie S, Strand C, Tachrount M, Thomas DL, Holton JL. Effect of Fluorinert on the Histological Properties of Formalin-Fixed Human Brain Tissue. *J Neuropathol Exp Neurol*. 2018;77(12):1085-1090.
 133. Stejskal EO, Tanner JE. Spin diffusion measurements: spin echoes in the presence of a time-dependent field gradient. *J Chem Phys*. 1965;42(1):288-292.
 134. McNab JA, Jbabdi S, Deoni SCL, Douaud G, Behrens TEJ, Miller KL. High resolution diffusion-weighted imaging in fixed human brain using diffusion-weighted steady state free precession. *Neuroimage*. 2009;46(3):775-785.
 135. Tendler BC, Foxley S, Cottaar M, Jbabdi S, Miller KL. Modeling an equivalent b-value in diffusion-weighted steady-state free precession. *Magn Reson Med*. 2020;84(2):873-884.
 136. Xu J, Does MD, Gore JC. Quantitative characterization of tissue microstructure with temporal diffusion spectroscopy. *J Magn Reson*. 2009;200(2):189-197.
 137. Colvin DC, Yankeelov TE, Does MD, Yue Z, Quarles C, Gore JC. New insights into tumor microstructure using temporal diffusion spectroscopy. *Cancer Res*. 2008;68(14):5941-5947.
 138. Topgaard D. Multidimensional diffusion MRI. *J Magn Reson*. 2017;275:98-113.
 139. Saleem KS, Avram AV, Glen D, et al. High-resolution mapping and digital atlas of subcortical regions in the macaque monkey based on matched MAP-MRI and histology. *Neuroimage*. 2021;245:118759.
 140. Bernstein M. A. KKFAZXJ. *Handbook of MRI Pulse Sequences*. Elsevier; 2004.
 141. Miller KL, Stagg CJ, Douaud G, et al. Diffusion imaging of whole, post-mortem human brains on a clinical MRI scanner. *Neuroimage*. 2011;57(1):167-181.
 142. Pfefferbaum A, Sullivan EV, Adalsteinsson E, Garrick T, Harper C. Postmortem MR imaging of formalin-fixed human brain. *NeuroImage*. 2004;21(4):1585-1595. doi:10.1016/j.neuroimage.2003.11.024
 143. Foxley S, Jbabdi S, Clare S, et al. Improving diffusion-weighted imaging of post-mortem human brains: SSFP at 7T. *NeuroImage*. 2014;102:579-589. doi:10.1016/j.neuroimage.2014.08.014
 144. Miller KL, McNab JA, Jbabdi S, Douaud G. Diffusion tractography of post-mortem human brains: optimization and comparison of spin echo and steady-state free precession techniques. *Neuroimage*. 2012;59(3):2284-2297.
 145. Henriques RN, Jespersen SN, Shemesh N. Correlation tensor magnetic resonance imaging. *Neuroimage*. 2020;211:116605.
 146. Chuhutin A, Hansen B, Jespersen SN. Precision and accuracy of diffusion kurtosis estimation and the influence of b-value selection. *NMR Biomed*. 2017;30(11):e3777.
 147. Maffei C, Girard G, Schilling KG, et al. Insights from the IronTract challenge: Optimal

- methods for mapping brain pathways from multi-shell diffusion MRI. *Neuroimage*. 2022;257:119327.
148. Wang H, Zhu J, Reuter M, et al. Cross-validation of serial optical coherence scanning and diffusion tensor imaging: a study on neural fiber maps in human medulla oblongata. *Neuroimage*. 2014;100:395-404.
 149. Schilling KG, Janve V, Gao Y, Stepniewska I, Landman BA, Anderson AW. Histological validation of diffusion MRI fiber orientation distributions and dispersion. *NeuroImage*. 2018;165:200-221. doi:10.1016/j.neuroimage.2017.10.046
 150. Grisot G, Haber SN, Yendiki A. Diffusion MRI and anatomic tracing in the same brain reveal common failure modes of tractography. *Neuroimage*. 2021;239:118300.
 151. Fieremans E, Lee HH. Physical and numerical phantoms for the validation of brain microstructural MRI: A cookbook. *Neuroimage*. 2018;182:39-61.
 152. Bammer R, Holdsworth SJ, Aksoy M, Skare ST. Phase Errors in Diffusion-Weighted Imaging. *Diffusion MRI*. 2010:218-249. doi:10.1093/med/9780195369779.003.0014
 153. Pizzolato M, Gilbert G, Thiran JP, Descoteaux M, Deriche R. Adaptive phase correction of diffusion-weighted images. *Neuroimage*. 2020;206:116274.
 154. van Schadewijk R, Krug JR, Shen D, et al. Magnetic Resonance microscopy at cellular resolution and localised spectroscopy of *Medicago truncatula* at 22.3 Tesla. *Sci Rep*. 2020;10(1):971.
 155. Tendler BC, Hanayik T, Ansorge O, et al. The Digital Brain Bank, an open access platform for post-mortem imaging datasets. *Elife*. 2022;11. doi:10.7554/eLife.73153
 156. Wang N, White LE, Qi Y, Cofer G, Johnson GA. Cytoarchitecture of the mouse brain by high resolution diffusion magnetic resonance imaging. *Neuroimage*. 2020;216:116876.
 157. Liang Z, Lee CH, Arefin TM, et al. Virtual mouse brain histology from multi-contrast MRI via deep learning. *Elife*. 2022;11. doi:10.7554/eLife.72331
 158. Johnson GA, Laoprasert R, Anderson RJ, et al. A multicontrast MR atlas of the Wistar rat brain. *Neuroimage*. 2021;242:118470.
 159. Chary K, Narvaez O, Salo RA, et al. Microstructural Tissue Changes in a Rat Model of Mild Traumatic Brain Injury. *Frontiers in Neuroscience*. 2021;15. doi:10.3389/fnins.2021.746214
 160. Dyrby TB, Lundell H, Burke MW, et al. Interpolation of diffusion weighted imaging datasets. *Neuroimage*. 2014;103:202-213.
 161. Ambrosen KS, Eskildsen SF, Hinne M, et al. Validation of structural brain connectivity networks: The impact of scanning parameters. *Neuroimage*. 2020;204:116207.
 162. Mars RB, Foxley S, Verhagen L, et al. The extreme capsule fiber complex in humans and macaque monkeys: a comparative diffusion MRI tractography study. *Brain Struct Funct*. 2016;221(8):4059-4071.

163. Howard AFD, Huszar IN, Smart A, et al. The BigMac dataset: an open resource combining multi-contrast MRI and microscopy in the macaque brain. *bioRxiv*. September 2022:2022.09.08.506363. doi:10.1101/2022.09.08.506363
164. Flint JJ, Hansen B, Fey M, et al. Cellular-level diffusion tensor microscopy and fiber tracking in mammalian nervous tissue with direct histological correlation. *Neuroimage*. 2010;52(2):556-561.
165. Flint JJ, Hansen B, Portnoy S, et al. Magnetic resonance microscopy of human and porcine neurons and cellular processes. *Neuroimage*. 2012;60(2):1404-1411.
166. Flint JJ, Lee CH, Hansen B, et al. Magnetic resonance microscopy of mammalian neurons. *Neuroimage*. 2009;46(4):1037-1040.
167. Portnoy S, Flint JJ, Blackband SJ, Stanisiz GJ. Oscillating and pulsed gradient diffusion magnetic resonance microscopy over an extended b-value range: implications for the characterization of tissue microstructure. *Magn Reson Med*. 2013;69(4):1131-1145.
168. Benveniste H, Blackband SJ. Translational neuroscience and magnetic-resonance microscopy. *Lancet Neurol*. 2006;5(6):536-544.
169. Ciobanu L. *Microscopic Magnetic Resonance Imaging: A Practical Perspective*. Jenny Stanford Publishing; 2017.
170. Winkler SA, Schmitt F, Landes H, et al. Gradient and shim technologies for ultra high field MRI. *Neuroimage*. 2018;168:59-70.
171. Anders J, Korvink JG. *Micro and Nano Scale NMR: Technologies and Systems*. John Wiley & Sons; 2018.
172. Raman MR, Shu Y, Lesnick TG, Jack CR, Kantarci K. Regional T1 relaxation time constants in Ex vivo human brain: Longitudinal effects of formalin exposure. *Magn Reson Med*. 2017;77(2):774-778.
173. Shatil AS, Uddin MN, Matsuda KM, Figley CR. Quantitative Ex Vivo MRI Changes due to Progressive Formalin Fixation in Whole Human Brain Specimens: Longitudinal Characterization of Diffusion, Relaxometry, and Myelin Water Fraction Measurements at 3T. *Front Med*. 2018;5:31.
174. Xiao J, Hornburg KJ, Cofer G, et al. A time-course study of actively stained mouse brains: Diffusion tensor imaging parameters and connectomic stability over 1 year. *NMR Biomed*. September 2021:e4611.